DrJes

Dawson Research Journal of Experimental Sciences

Winter 2026

Volume 16

Features

About the Cover

The cover of this issue was submitted by Tristan Peirce, a Health Science student, with the following caption:

"If you were to stand directly on the equator, the Earth would spin you around its rotational axis at more than 1600 km/hr. As you move towards either pole, this tangential velocity decreases and decreases until you reach zero, at which point you have arrived at the pole. Despite how fast this is, on the surface of the Earth, it can be difficult to discern our speed. Astrophotography can help us visualise this constant spinning.

Captured during a fall field trip to Arundel, Quebec, with the Dawson Environmental Sciences cohort, this image was created by stacking 200 exposures taken over one hour, with the camera pointed north. The resulting star trails reveal the apparent rotation of the night sky, tracing arcs around Polaris. Positioned nearly in line with Earth's axis, Polaris appears almost fixed, anchoring the swirling motion around it, giving it the nickname of the North Star."

Letter from the Editors

Welcome to this sixteenth edition of the *Dawson Journal of Experimental Science* (*DrJes*). We are pleased to share a selection of work that reflects the effort, curiosity, and persistence of the Dawson students who contributed to this publication. Each article represents more than a final result. It captures a lengthy but rewarding process of questioning, testing, and refining ideas over time.

One of the most striking aspects of this issue is the range of approaches taken by the authors who went beyond the regular Science program curriculum. Some projects focus on careful measurement and analysis, while others explore broader questions through creative experimental design. In each case, what stands out is a genuine engagement with the scientific method. The work presented here shows that meaningful learning often comes from uncertainty, revision, and thoughtful interpretation rather than from immediate success. We hope that this quest for knowledge will inspire you, dear Readers, to pursue your own scientific endeavours and contribute to the larger scientific dialogue.

Editing this journal has also highlighted the importance of collaboration. Many of these projects were shaped through discussion with peers and insightful guidance from instructors. This shared effort contributes to a stronger and more thoughtful scientific community within Dawson.

Finally, we would like to thank all contributors, reviewers, and faculty members for their generous time and unwavering dedication. Their involvement makes this journal possible and continues to raise its quality. We would like to end by thanking our team of editors who took valuable time out of their already schedule to reach out to referees, format, and edit each article thoroughly, ensuring a high-quality journal for you to enjoy.

Happy reading!

Thomas Deleuze Bisson
Emeline Tchung
Head Editors, DrJes (2025-2026)

Editors

Alexey Solovyev, Ariadni Lianidaki, Chloe Larivée, Kaylen Esquivel Kearns, Mani Sadeghi, Matthew Balas, Maya Kaci, Nadira Zibirov, Victor Chobadingedui, Martin Nguyen (social media manager).

Check out our Instagram:

@drjes_2024

Email for article submissions:

drjeseditorial@gmail.com

Contents

Referees

A Theoretical Framework for Neuroprotection: Human-Adapted Tardigrade Damage Suppressor Protein Engineering and mRNA-Based Delivery for PTSD and Alzheimer's Disease

MD Ahlam Hamid, Aryan Shadzi, John Mikhael[1], Logan James Nguyen Huu

[1] Champlain College Saint-Lambert, Saint-Lambert, Quebec

Abstract — Post-traumatic stress disorder (PTSD) affects 4% globally (WHO, 2024), and Alzheimer's disease (AD) impacts 1 in 9 seniors above 65 years of age (Alzheimer's Association, n.d.). Both are linked to oxidative stress (Huang et al., 2016; Karanikas et al., 2021), yet current treatments fail to halt progression (Miculas et al., 2022). Tardigrade damage suppressor (Dsup) proteins shield DNA from hydroxyl radicals but induce toxic chromatin condensation in human neurons (Escarcega et al., 2023). This paper proposes a human-adapted Dsup variant with targeted C-terminal lysine/arginine substitutions to reduce charge density. We outline a dual-mRNA strategy using separate transcripts for nuclear and mitochondrial targeting, produced via in vitro transcription (IVT) with N^1-methylpseudouridine-modified ($m1\psi$) mRNA modifications (Sahin et al., 2014; Ho et al., 2024) and delivered via ApoE-functionalized lipid nanoparticles (LNPs) for blood-brain barrier penetration (Magro et al., 2017). Evaluation in induced pluripotent stem cell (iPSC)-derived neurons focuses on reducing $\gamma H2AX$ foci without chromatin disruption (Escarcega et al., 2023), supporting that this strategy can potentially be a future treatment for oxidative stress-related neurological conditions.

Introduction

Shared Mechanisms in PTSD and Alzheimer's Disease

Both PTSD and Alzheimer's disease (AD) fundamentally disrupt memory, emotional regulation, and cognitive function. PTSD arises from traumatic exposure, while AD is characterized by progressive loss of synaptic connections and modified gene expression (Shankar & Walsh, 2009; Meftah & Gan, 2023). Despite their differences, both conditions stem from similar underlying factors, including neurotransmitter imbalances, inflammation, epigenetic changes, and oxidative stress.

Neurotransmitter dysregulation involves excessive release of glutamate, dopamine, and norepinephrine during trauma, strengthening fear-related memory encoding (Azevedo et al., 2024; Ouyang et al., 2012). Glutamate acts on NMDA and AMPA receptors, causing excitotoxicity that shrinks dendrites and reduces synapse count, particularly in the hippocampus and the prefrontal cortex (McEwen, 2017; Rivera-Cervantes et al., 2014). Decreased gamma-aminobutyric acid (GABA) levels contribute to circuit hyperexcitability and anxiety (Ghosal et al., 2016).

Dysfunction of the hypothalamic–pituitary–adrenal (HPA) axis disrupts cortisol regulation through altered glucocorticoid receptor signaling. Chronic trauma causes HPA axis hyperactivity or hypoactivity, damaging the hippocampus and the amygdala while disrupting brain-derived neurotrophic factor (BDNF) necessary for neuron health (Karin, O. et al., 2020; Kaur et al., 2025; Knezevic et al., 2023; Seo et al., 2018; Deppermann et al., 2014).

When microglia and astrocytes become activated, they trigger neuroinflammation that releases inflammatory molecules, which in turn harm synaptic connections. Dendritic spines are lost due to decreased synaptic proteins (Karve et al., 2015; Jarrahi et al., 2020; Merino-Serrais et al., 2018). Epigenetic modifications, including histone modification and DNA methylation, further lower BDNF expression, increasing brain vulnerability to stress (Golubeva et al., 2024; Zhao et al., 2020).

Oxidative stress, characterized by imbalance between free radicals and antioxidants, represents a critical driver (Miller & Sadeh, 2014). Reactive oxygen species (ROS) and reactive nitrogen species (RNS), particularly hydroxyl radicals, react with DNA, lipids, and proteins (Chandimali et al., 2025). Hydroxyl radicals specifically react with hydrogen in deoxyribose, weakening DNA structure and leading to neuronal apoptosis (Balasubramanian et al., 1998). Chronic glucocorticoid exposure generates additional ROS, accelerating aging-like neuronal damage observed in both conditions (Torres et al., 2021; Jamjoom et al., 2020), a process significantly driven by hydroxyl radical attack on DNA (Figure 1).

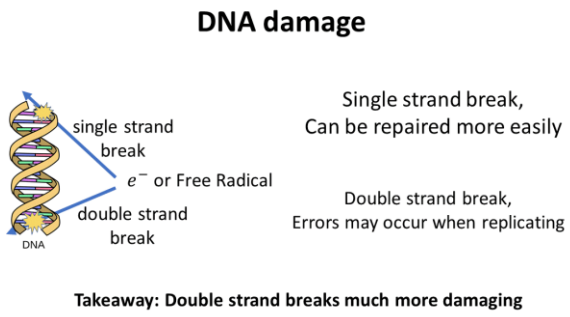

Figure 1. Effects of free radicals on DNA (Nett, 2020).

These failures in cellular function gradually impair cognition (Figure 2), creating heavy personal and social burdens. Gaining a clearer understanding of the underlying mechanisms could guide the development of new treatments inspired by the resilience of tardigrade proteins.

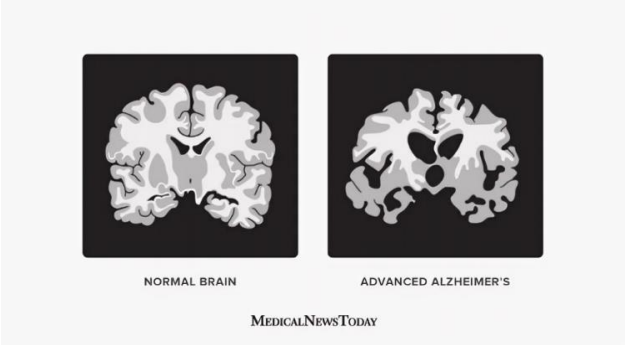

Figure 2. Normal vs advanced AD brain (Morales-Brown, 2024).

Tardigrade Damage Suppressor Protein

Tardigrades, or colloquially known as "water bears" (Figure 3), show extreme resistance to pressure, temperature, and ionizing radiation. This resilience is driven by their genome, which encodes protective proteins such as Cytosolic Abundant Heat Soluble (CAHS), Secretory Abundant Heat Soluble (SAHS), and Damage Suppressor (Dsup) proteins. Notably, the species *Ramazzottius varieornatus* can survive up to 5,000 Gy of gamma radiation, which exceeds the median lethal dose for humans by more than 1,000 times (Hashimoto et al., 2016).

Figure 3. Image of a tardigrade (also known as "water bears") under a microscope (Weisberger & Ghose, 2024).

The tardigrade Dsup protein is intrinsically disordered and highly flexible. Its amino acid-rich C-terminal region is responsible for nuclear localization and nucleosome binding (Mínguez-Toral et al., 2020). Dsup contains regions homologous to vertebrate High Mobility Group Nucleosome (HMGN) binding proteins, which anchor it to chromatin (Chavez et al., 2019; Caswell, 2023). When bound to DNA, Dsup alters chromatin structural organization and forms a physical barrier over the minor groove, which strengthens the DNA helix.

This shielding limits contact between hydroxyl radicals, generated by the irradiation of water molecules, and the

deoxyribose-phosphate backbone of DNA, thereby reducing oxidative stress and preventing DNA double strand breaks (Hashimoto & Kunieda, 2017; Hashimoto et al., 2016). Experiments in human embryonic kidney (HEK 293T) cells have successfully demonstrated this protective effect, Dsup-expressing cells show fewer DNA double-strand breaks after X-ray exposure compared to untreated cells (Hashimoto et al., 2016).

Mechanistic Limitations of the Damage Suppressor Protein in Human Neurons

Despite its protective effects, direct use of Dsup in human neurons poses major limitations. Dsup has no fixed structure and binds to chromatin non-specifically through strong electrostatic attraction between its alkaline C-terminal region and the negatively charged DNA backbone (Hashimoto et al., 2016).

This interaction shields DNA from damage by blocking ROS and hydroxyl radicals, but it also induces toxicity. Since Dsup binds in a non-specific way, it lacks the specificity to differentiate between DNA regions that require protection from those that need to stay open for essential processes such as transcription, replication, and repair. As a result, Dsup causes chromatin condensation, disrupting the three-dimensional organization of neuronal chromatin and interfering with genomic communication and cellular homeostasis (Medrano-Fernández & Barco, 2016; Escarcega et al., 2023).

In sensitive cell types such as neurons, this disruption fails to provide protection. Instead, it interferes with DNA-dependent signaling pathways, increasing DNA damage, impairing transcription, and triggering neurotoxicity (Escarcega et al., 2023). To address this, Dsup could be redesigned in principle as a human-adapted variant that preserves DNA protection while limiting interference with chromatin structure. Modifying its mRNA sequence may also reduce harmful condensation and enable targeted delivery within the cell, potentially extending protection beyond the nucleus and providing a broader theoretical basis for defense against hydroxyl radical-induced damage.

Experimental Framework

mRNA Design and Lipid Nanoparticle Delivery

mRNA-encapsulated lipid nanoparticles (LNPs) allow the delivery of engineered Dsup variants to neurons, reducing neurotoxicity and allowing targeting of precise organelles (Torkzaban et al., 2025).

Experimental Protocol and Molecular Design

Transient, Non-Genomic Delivery Method

The delivery of the modified Dsup variant into human neurons uses a transient, non-genomic method based on synthetic messenger RNA (mRNA). This method avoids permanent genomic integration by applying controlled in vitro transcription (IVT), which enables temporary expression and is generally considered safer for early-stage molecular testing (Sahin et al., 2014). Because mRNA delivery is non-integrative, the protective effects of the modified protein can be evaluated without altering the cell's native DNA.

Structural Engineering of the Damage Suppressor Protein

The native Dsup protein from *Ramazzottius varieornatus* binds to nucleosomes to shield DNA, but in human neurons it can trigger chromatin condensation and DNA damage (Chavez et al., 2019; Escarcega et al., 2023). To counter these effects, the C-terminal region of the native *R. varieornatus* Dsup protein is modified to reduce its positive charge density. This is achieved by identifying highly basic clusters of lysine (K) and arginine (R) residues and substituting them with neutral amino acids, such as alanine (A) or serine (S) via site-directed mutagenesis of the template DNA (Urabe et al., 1999). This reduction in alkalinity limits the electrostatic binding to the negatively charged DNA backbone that otherwise drives chromatin condensation.

To ensure protection across organelles, this framework suggests delivering two separate mRNAs: one encoding a Nuclear-Targeted Dsup with a C-terminal Nuclear Localization Signal (NLS) to protect genomic DNA, and another encoding a Mitochondrial-Targeted Dsup with an N-terminal Mitochondrial Targeting Signal (MTS) to protect mitochondrial DNA (mtDNA) and reduce ROS-related cell damage. Using two mRNAs avoids competition between targeting signals that could happen with a single protein, allowing both versions to work efficiently in their respective organelles (Chavez et al., 2019).

Synthetic mRNA Optimization

During the IVT process, the synthetic mRNA incorporates N^1-methylpseudouridine ($m1\psi$) to increase translational efficiency. This modification significantly reduces the

activation of Toll-like receptors (TLR7/8), minimizing the risk of an innate immune response in sensitive neuronal tissues (Sahin et al., 2014; Ho et al., 2024). These optimizations enhance both the stability and compatibility of the engineered transcript.

Lipid Nanoparticle Formulation and Brain Delivery

The modified mRNA is encapsulated in ionizable lipid nanoparticles (LNPs) to prevent degradation and facilitate cellular uptake. Surface ligand functionalization using Apolipoprotein E (ApoE) or transferrin enables receptor-mediated transcytosis across the blood-brain barrier, allowing efficient neuronal delivery (Hou et al., 2021; Topal et al., 2020). Alternatively, intranasal administration through olfactory and trigeminal pathways provides non-invasive access to the brain (Li et al., 2025).

Validation in Neurons

Evaluation of the modified construct occurs in induced pluripotent stem cell (iPSC)-derived human neurons. Successful expression would be defined as a reduction in the DNA double-strand break marker $\gamma H2AX$ following oxidative stress, with no evidence of chromatin condensation or reduced transcriptional accessibility (Escarcega et al., 2023; Kinner et al., 2008).

Expected Outcome

The modified Dsup variant is expected in principle to reduce oxidative DNA damage in human neurons without inducing chromatin condensation or transcriptional disruption. In iPSC-derived neuronal models, expression of the charge-reduced variant is hypothesized to result in lower $\gamma H2AX$ foci following oxidative stress, indicating enhanced genomic stability through a non-toxic physical shield. The dual-mRNA targeting strategy is expected to provide a measurable advantage over native Dsup by protecting both the nuclear and mitochondrial genomes. Mitochondrial targeting may additionally decrease reactive oxygen species leakage and prevent the initiation of mitochondrial-dependent apoptosis. Overall, such findings would help validate a human-compatible, mRNA-delivered Dsup as a conceptual candidate strategy for addressing oxidative stress-related neurological disorders.

Conclusion

This research proposes a modified, human-adapted variant of the tardigrade Damage Suppressor (Dsup) protein as a novel theoretical approach to mitigate oxidative DNA damage underlying PTSD and Alzheimer's disease. By employing synthetic mRNA delivery and targeted charged-to-alanine mutagenesis, the redesigned Dsup aims to preserve genomic stability without disrupting the 3D chromatin architecture essential for neuronal health. The integration of distinct nuclear and mitochondrial targeting sequences via a co-delivery mRNA platform enhances protection across key neuronal organelles, while lipid nanoparticle functionalization ensures accessibility across the blood-brain barrier.

Collectively, this work outlines a feasible conceptual strategy for translating extremophile-derived resilience mechanisms into human neuroprotection. While further validation would be required to confirm long-term safety and efficacy, the framework establishes a conceptual foundation for future therapies for oxidative stress in neurodegenerative and trauma-related disorders. Since this framework modifies neuronal DNA damage responses and mitochondrial function, any future experimental application would need thorough ethical and safety review in preclinical models.

Acknowledgements

This project was initiated at École internationale Lucille-Teasdale under the supervision of our chemistry teacher Geanina Cotirgasanu as part of the miniGEM competition hosted by McGill University.

References

[1] *Alzheimer's Disease facts and figures*. (n.d.). Alzheimer's Association. https://www.alz.org/alzheimers-dementia/facts-figures

[2] Azevedo, M., Martinho, R., Oliveira, A., Correia-De-Sá, P., & Moreira-Rodrigues, M. (2024). Molecular pathways underlying sympathetic autonomic overshooting leading to fear and traumatic memories: looking for alternative therapeutic options for post-traumatic stress disorder. *Frontiers in Molecular Neuroscience, 16*, 1332348. https://doi.org/10.3389/fnmol.2023.1332348

[3] Balasubramanian, B., Pogozelski, W. K., & Tullius, T. D. (1998). DNA strand breaking by the hydroxyl radical is governed by the accessible surface areas of the hydrogen atoms of the DNA backbone.

Proceedings of the National Academy of Sciences, 95(17), 9738–9743. https://doi.org/10.1073/pnas.95.17.9738

[4] Caswell, G. (2023). *A Human-Optimized Damage Suppressor Protein as a Potential Tool to Improve DNA Damage Protection in Human Cells*. https://escholarship.org/content/qt0k86n8f2/qt0k86n8f2_noSplash_ff2143244a401d225ac7b8d341e387e7.pdf

[5] Chandimali, N., Bak, S. G., Park, E. H., Lim, H., Won, Y., Kim, E., Park, S., & Lee, S. J. (2025). Free radicals and their impact on health and antioxidant defenses: a review. *Cell Death Discovery, 11*(1), 19. https://doi.org/10.1038/s41420-024-02278-8

[6] Chavez, C., Cruz-Becerra, G., Fei, J., Kassavetis, G. A., & Kadonaga, J. T. (2019). The tardigrade damage suppressor protein binds to nucleosomes and protects DNA from hydroxyl radicals. *eLife, 8*. https://doi.org/10.7554/elife.47682

[7] Deppermann, S., Storchak, H., Fallgatter, A., & Ehlis, A. (2014). Stress-induced neuroplasticity: (Mal)adaptation to adverse life events in patients with PTSD – A critical overview. *Neuroscience, 283*, 166–177. https://doi.org/10.1016/j.neuroscience.2014.08.037

[8] Escarcega, R. D., Patil, A. A., Meyer, M. D., Moruno-Manchon, J. F., Silvagnoli, A. D., McCullough, L. D., & Tsvetkov, A. S. (2023). The Tardigrade damage suppressor protein Dsup promotes DNA damage in neurons. *Molecular and Cellular Neuroscience, 125*, 103826. https://doi.org/10.1016/j.mcn.2023.103826

[9] Ghosal, S., Hare, B. D., & Duman, R. S. (2016). Prefrontal cortex GABAergic deficits and circuit dysfunction in the pathophysiology and treatment of chronic stress and depression. *Current Opinion in Behavioral Sciences, 14*, 1–8. https://doi.org/10.1016/j.cobeha.2016.09.012

[10] Golubeva, E., Zeltser, A., Zorkina, Y., Ochneva, A., Tsurina, A., Andreyuk, D., Kostyuk, G., & Morozova, A. (2024). Epigenetic Alterations in Post-Traumatic Stress Disorder: Comprehensive Review of Molecular Markers. *Complex Psychiatry, 10*(1–4), 71–107. https://doi.org/10.1159/000541822

[11] Hashimoto, T., Horikawa, D. D., Saito, Y., Kuwahara, H., Kozuka-Hata, H., Shin-I, T., Minakuchi, Y., Ohishi, K., Motoyama, A., Aizu, T., Enomoto, A., Kondo, K., Tanaka, S., Hara, Y., Koshikawa, S., Sagara, H., Miura, T., Yokobori, S., Miyagawa, K., . . . Kunieda, T. (2016). Extremotolerant tardigrade genome and improved radiotolerance of human cultured cells by tardigrade-unique protein. *Nature Communications, 7*(1), 12808. https://doi.org/10.1038/ncomms12808

[12] Hashimoto, T., & Kunieda, T. (2017). DNA Protection Protein, a Novel Mechanism of Radiation Tolerance: Lessons from Tardigrades. *Life, 7*(2), 26. https://doi.org/10.3390/life7020026

[13] Ho, L. L. Y., Schiess, G. H. A., Miranda, P., Weber, G., & Astakhova, K. (2024). Pseudouridine and N1-methylpseudouridine as potent nucleotide analogues for RNA therapy and vaccine development. *RSC Chemical Biology, 5*(5), 418–425. https://doi.org/10.1039/d4cb00022f

[14] Hou, X., Zaks, T., Langer, R., & Dong, Y. (2021). Lipid nanoparticles for mRNA delivery. *Nature Reviews Materials, 6*(12), 1078–1094. https://doi.org/10.1038/s41578-021-00358-0

[15] Huang, W., Zhang, X., & Chen, W. (2016). Role of oxidative stress in Alzheimer's disease. *Biomedical Reports, 4*(5), 519–522. https://doi.org/10.3892/br.2016.630

[16] Jamjoom, A. a. B., Rhodes, J., Andrews, P. J. D., & Grant, S. G. N. (2020). The synapse in traumatic brain injury. *Brain, 144*(1), 18–31. https://doi.org/10.1093/brain/awaa321

[17] Jarrahi, A., Braun, M., Ahluwalia, M., Gupta, R. V., Wilson, M., Munie, S., Ahluwalia, P., Vender, J. R., Vale, F. L., Dhandapani, K. M., & Vaibhav, K. (2020). Revisiting traumatic brain injury: From molecular mechanisms to therapeutic interventions. *Biomedicines, 8*(10), 389. https://doi.org/10.3390/biomedicines8100389

[18] Karanikas, E., Daskalakis, N. P., & Agorastos, A. (2021). Oxidative Dysregulation in Early Life Stress and Posttraumatic Stress Disorder: A Comprehensive review. *Brain Sciences, 11*(6), 723. https://doi.org/10.3390/brainsci11060723

[19] Karin, O., Raz, M., Tendler, A., Bar, A., Korem Yael, K., Milo, T., & Alon, U. (2020). A new model for the HPA axis explains dysregulation of stress hormones on the timescale of weeks. *Molecular Systems Biology, 16*, e9510. https://doi.org/10.15252/msb.20209510

[20] Karve, I. P., Taylor, J. M., & Crack, P. J. (2015). The contribution of astrocytes and microglia to traumatic

brain injury. *British Journal of Pharmacology, 173*(4), 692–702. https://doi.org/10.1111/bph.13125

[21] Kaur, J., Gandhi, J., & Sharma, S. (2025, December 1). *Physiology, cortisol*. StatPearls - NCBI Bookshelf. https://www.ncbi.nlm.nih.gov/books/NBK538239/

[22] Kinner, A., Wu, W., Staudt, C., & Iliakis, G. (2008). $\gamma H2AX$ in recognition and signaling of DNA double-strand breaks in the context of chromatin. *Nucleic Acids Research, 36*(17), 5678–5694. https://doi.org/10.1093/nar/gkn550

[23] Knezevic, E., Nenic, K., Milanovic, V., & Knezevic, N. N. (2023). The role of cortisol in chronic stress, neurodegenerative diseases, and psychological disorders. *Cells, 12*(23), 2726. https://doi.org/10.3390/cells12232726

[24] Li, H., Shen, X., Zhang, B., Li, Y., Alexander, C., Harvey, P., & Zhu, Z. (2025). Brain-targeted intranasal delivery of biologics: a perspective for Alzheimer's disease treatment. *RSC Pharmaceutics, 2*(6), 1323–1348. https://doi.org/10.1039/d5pm00148j

[25] Magro, R. D., Ornaghi, F., Cambianica, I., Beretta, S., Re, F., Musicanti, C., Rigolio, R., Donzelli, E., Canta, A., Ballarini, E., Cavaletti, G., Gasco, P., & Sancini, G. (2017). ApoE-modified solid lipid nanoparticles: A feasible strategy to cross the blood-brain barrier. *Journal of Controlled Release, 249,* 103–110. https://doi.org/10.1016/j.jconrel.2017.01.039

[26] McEwen, B. S. (2017). Neurobiological and systemic effects of chronic stress. *Chronic Stress, 1*. https://doi.org/10.1177/2470547017692328

[27] Medrano-Fernández, A., & Barco, A. (2016). Nuclear organization and 3D chromatin architecture in cognition and neuropsychiatric disorders. *Molecular Brain, 9*(1), 83. https://doi.org/10.1186/s13041-016-0263-x

[28] Meftah, S., & Gan, J. (2023). Alzheimer's disease as a synaptopathy: Evidence for dysfunction of synapses during disease progression. *Frontiers in Synaptic Neuroscience, 15,* 1129036. https://doi.org/10.3389/fnsyn.2023.1129036

[29] Merino-Serrais, P., Loera-Valencia, R., Rodriguez-Rodriguez, P., Parrado-Fernandez, C., Ismail, M. A., Maioli, S., Matute, E., Jimenez-Mateos, E. M., Björkhem, I., DeFelipe, J., & Cedazo-Minguez, A. (2018). 27-Hydroxycholesterol induces aberrant morphology and synaptic dysfunction in hippocampal neurons. *Cerebral Cortex, 29*(1), 429–446. https://doi.org/10.1093/cercor/bhy274

[30] Miculas, D. C., Negru, P. A., Bungau, S. G., Behl, T., Hassan, S. S. U., & Tit, D. M. (2022). Pharmacotherapy evolution in Alzheimer's Disease: Current framework and relevant directions. *Cells, 12*(1), 131. https://doi.org/10.3390/cells12010131

[31] Miller, M. W., & Sadeh, N. (2014). Traumatic stress, oxidative stress and post-traumatic stress disorder: neurodegeneration and the accelerated-aging hypothesis. *Molecular Psychiatry, 19*(11), 1156–1162. https://doi.org/10.1038/mp.2014.111

[32] Mínguez-Toral, M., Cuevas-Zuviría, B., Garrido-Arandia, M., & Pacios, L. F. (2020). A computational structural study on the DNA-protecting role of the tardigrade-unique Dsup protein. *Scientific Reports, 10*(1), 13424. https://doi.org/10.1038/s41598-020-70431-1

[33] Morales-Brown, P. (2024, March 22). *Alzheimer's brain vs. normal brain: What to know*. https://www.medicalnewstoday.com/articles/alzheimers-brain-vs-normal-brain

[34] Nett, B., PhD. (2020, November 19). *Radiation Biology Illustrated Introduction [ionization DNA Breaks, LD50, Stochastic Vs Deterministic] For*. How Radiology Works. https://howradiologyworks.com/radiationbiology/

[35] Ouyang, M., Young, M. B., Lestini, M. M., Schutsky, K., & Thomas, S. A. (2012). Redundant catecholamine signaling consolidates fear memory via phospholipase C. *Journal of Neuroscience, 32*(6), 1932–1941. https://doi.org/10.1523/jneurosci.5231-11.2012

[36] Rivera-Cervantes, M. C., Castañeda-Arellano, R., Castro-Torres, R. D., Gudiño-Cabrera, G., Velasco, A. I. F. Y., Camins, A., & Beas-Zárate, C. (2014). P38 MAPK inhibition protects against glutamate neurotoxicity and modifies NMDA and AMPA receptor subunit expression. *Journal of Molecular Neuroscience, 55*(3), 596–608. https://doi.org/10.1007/s12031-014-0398-0

[37] Sahin, U., Karikó, K., & Türeci, Ö. (2014). mRNA-based therapeutics — developing a new class of drugs. *Nature Reviews Drug Discovery, 13*(10), 759–780. https://doi.org/10.1038/nrd4278

[38] Seo, D., Rabinowitz, A. G., Douglas, R. J., & Sinha, R. (2018). Limbic response to stress linking life

trauma and hypothalamus-pituitary-adrenal axis function. *Psychoneuroendocrinology, 99*, 38–46. https://doi.org/10.1016/j.psyneuen.2018.08.023

[39] Shankar, G. M., & Walsh, D. M. (2009). Alzheimer's disease: synaptic dysfunction and Aβ. *Molecular Neurodegeneration, 4*(1), 48. https://doi.org/10.1186/1750-1326-4-48

[40] Topal, G. R., Mészáros, M., Porkoláb, G., Szecskó, A., Polgár, T. F., Siklós, L., Deli, M. A., Veszelka, S., & Bozkir, A. (2020). ApoE-Targeting Increases the Transfer of Solid Lipid Nanoparticles with Donepezil Cargo across a Culture Model of the Blood–Brain Barrier. *Pharmaceutics, 13*(1), 38. https://doi.org/10.3390/pharmaceutics13010038

[41] Torkzaban, B., Zhu, Y., Lopez, C., Alexander, J. M., Ma, J., Sun, Y., Maschhoff, K. R., Hu, W., Jacob, M. H., Lin, D., Mao, H., Martin, S., & Coller, J. (2025). Use of polyadenosine tail mimetics to enhance mRNA expression from genes associated with haploinsufficiency disorders. *Molecular Therapy — Nucleic Acids, 36*(1), 102453. https://doi.org/10.1016/j.omtn.2025.102453

[42] Torres, D. J., Alfulaij, N., & Berry, M. J. (2021). Stress and the brain: an emerging role for selenium. *Frontiers in Neuroscience, 15*, 666601. https://doi.org/10.3389/fnins.2021.666601

[43] Urabe, M., Hasumi, Y., Kume, A., Surosky, R. T., Kurtzman, G. J., Tobita, K., & Ozawa, K. (1999). Charged-to-Alanine scanning mutagenesis of the N-Terminal half of Adeno-Associated virus Type 2 Rep78 protein. *Journal of Virology, 73*(4), 2682–2693. https://doi.org/10.1128/jvi.73.4.2682-2693.1999

[44] Weisberger, M., & Ghose, T. (2024, September 12). *Tardigrades: Facts about one of the hardiest animals on Earth, and beyond*. Live Science. https://www.livescience.com/57985-tardigrade-facts.html

[45] World Health Organization: WHO. (2024, May 27). *Post-traumatic stress disorder*. https://www.who.int/news-room/fact-sheets/detail/post-traumatic-stress-disorder

[46] Zhao, M., Wang, W., Jiang, Z., Zhu, Z., Liu, D., & Pan, F. (2020). Long-Term effect of post-traumatic stress in adolescence on dendrite development and H3K9ME2/BDNF expression in male rat hippocampus and prefrontal cortex. *Frontiers in Cell and Developmental Biology, 8*, 682. https://doi.org/10.3389/fcell.2020.00682

Banana Peel-Based Bioplastics: Combating Plastic Pollution and Food Waste Simultaneously

Maya Kaci, Lama Abdelmaged, Nadira Zibirov

Abstract – The overproduction and mismanagement of plastics, coupled with increasing food waste, have created severe environmental and health challenges, including ocean pollution, microplastic contamination, and elevated carbon emissions. Banana peels, a high-starch by-product of one of the world's most consumed fruits, present a sustainable raw material for bioplastic production. In this study, banana peel starch was extracted and combined with glycerol as a plasticizer to produce biodegradable films with enhanced flexibility and strength. The preparation involved acid treatment, glycerol addition, pH adjustment, casting, and drying to obtain functional bioplastic films. This approach not only reduces agricultural waste but also provides an eco-friendly alternative to conventional plastics, addressing both plastic pollution and food waste issues. The resulting banana peel-based bioplastics demonstrate promising mechanical properties, highlighting their potential for sustainable applications in packaging and other industries.

Introduction

We became immortal through plastic, one of humankind's biggest dreams came true and this long desired immortality is the cause of our ecosystem's downfall [1]. More than 430 million tons of plastic were produced in 2024, from which 11 million metric tons of plastic entered our oceans. According to Nicola Simpson, head of the United Nations Development Programme's Barbados and Eastern Caribbean Blue Economy Accelerator Lab: "there will be more plastic than fish in the ocean by mid-century" [2].

The UNEP estimates that plastic production, use, and disposal will account for 19% of the total global carbon budget by 2040. It is also the cause of multiple diseases. According to Augustina Besada, co-founder and CEO of Unplastify, an organization committed to ending plastic pollution, some of the microplastics, despite being tiny in size, "have been linked to possibly being cancerous." More than 900 health professionals and medical associations confirm that statement [2].

Little Wonder OXFAM called the COVID-19 pandemic "the hunger virus." This era has been marked by food waste that probably played a role in our climate crises. Additionally, Thomson Reuters Foundation warned in 2018 that "due to the increase in the world population and changing habits in the developing nations, food waste could rise by almost a third by 2030 when more than 2 billion tons of food will be thrown away" [3].

This crisis stems from our excessive consumption of plastic, its harmful impact on the climate, and its significant contribution to the growing levels of pollution. At the same time, food waste has increased each year, particularly since the global pandemic, which forced many of us to remain at home and consume more than necessary. Together, these issues demand urgent action and sustainable solutions to reduce the ecological problems our world is facing. If we fail to respond, future generations may no longer be able to live in the world as we once knew it.

Bananas are the fourth most important commodity after rice, wheat, and maize. India leads global production, averaging approximately 29.78 million tons from an area of 0.83 million ha. The peels, a major by-product of banana processing,

contain a high starch content (20-39%), making them a valuable raw material for various industrial uses, including biofuels, biosorbents, and bioplastics (Ravi and Mustaff, 2013) [4]. Banana peel waste amounts reach approximately 3.5 million tons annually and can take two years to biodegrade [5].

Glycerol is commonly used as a plasticizer because of its strong compatibility and hydrophilic nature that helps biofilms reduce their rigidity and achieve great flexibility and elasticity [6].

In our experiment, building on the role of glycerol, we will incorporate it into banana peel starch to produce a bioplastic film with improved flexibility and strength. This approach allows us to transform banana waste into a functional, biodegradable material, directly addressing plastic pollution and food waste problems.

Materials and Method

Preparation of Raw Materials

Banana peels were collected from fresh bananas and washed thoroughly with water to remove dirt and residues. The peels were cut into small pieces to increase surface area and blended with an appropriate amount of distilled water until a smooth paste was obtained.

Figure 1. Banana peels cut into small pieces prior to blending.

Figure 2. Banana peels after being blended, forming a smooth paste.

Preparation of Bioplastic

15 g of banana peel paste was weighed and placed in a 400 mL beaker. 15 mL of 0.1 M hydrochloric acid (HCl) was measured using a graduated cylinder, added to the beaker, and stirred with a glass stirring rod. Approximately 3 mL of glycerol, used as a plasticizer, was added and stirred to improve elasticity, followed by 10 mL of 0.1 M sodium hydroxide (NaOH). Additionally, 9 mL of cornstarch mixed with 6 mL of distilled water was added to the beaker to reduce dryness. The mixture was stirred thoroughly and spread on parchment paper placed on a watch glass. It was then heated in an oven at 150 °C for 45 minutes. After removal from the oven, the bioplastic was left to dry at room temperature for 24 hours.

Figure 3. Mixture of banana peel paste, HCl, glycerol, NaOH, and cornstarch stirred in a 400 mL beaker.

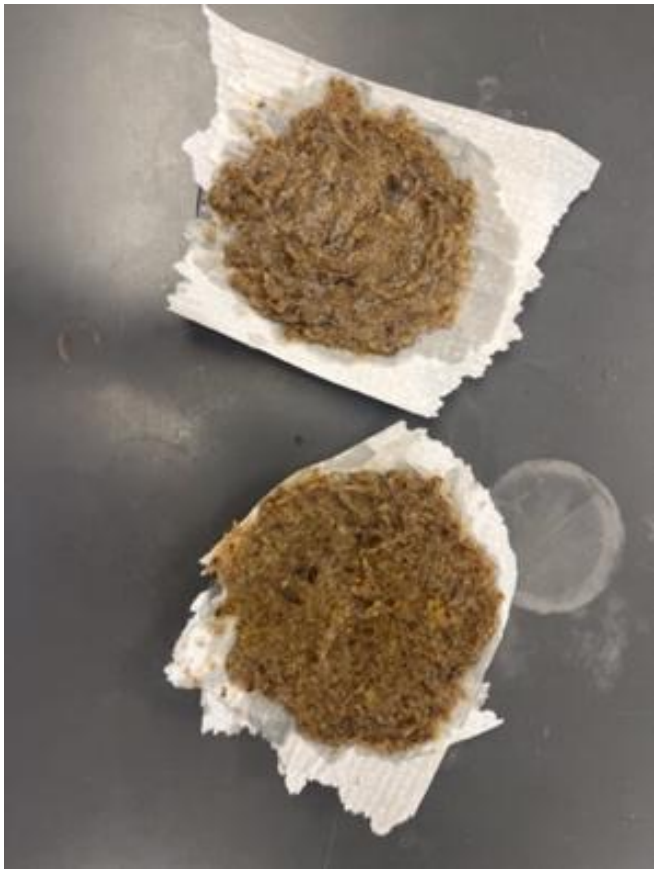

Figure 4. Prepared mixture spread evenly onto paper placed on a watch glass.

Figure 5. Banana peel paste mixture heated in an oven at 150°C for 45 minutes.

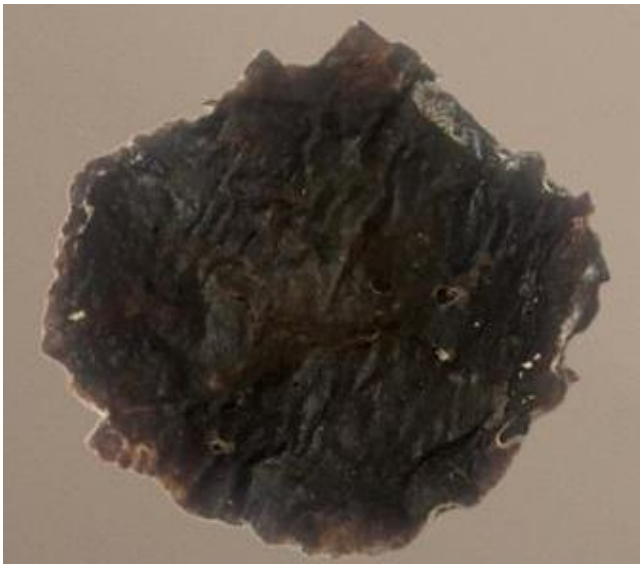

Figure 6. Fully dried banana peel-based bioplastic after 24 hours.

Microscopic View of Bioplastic

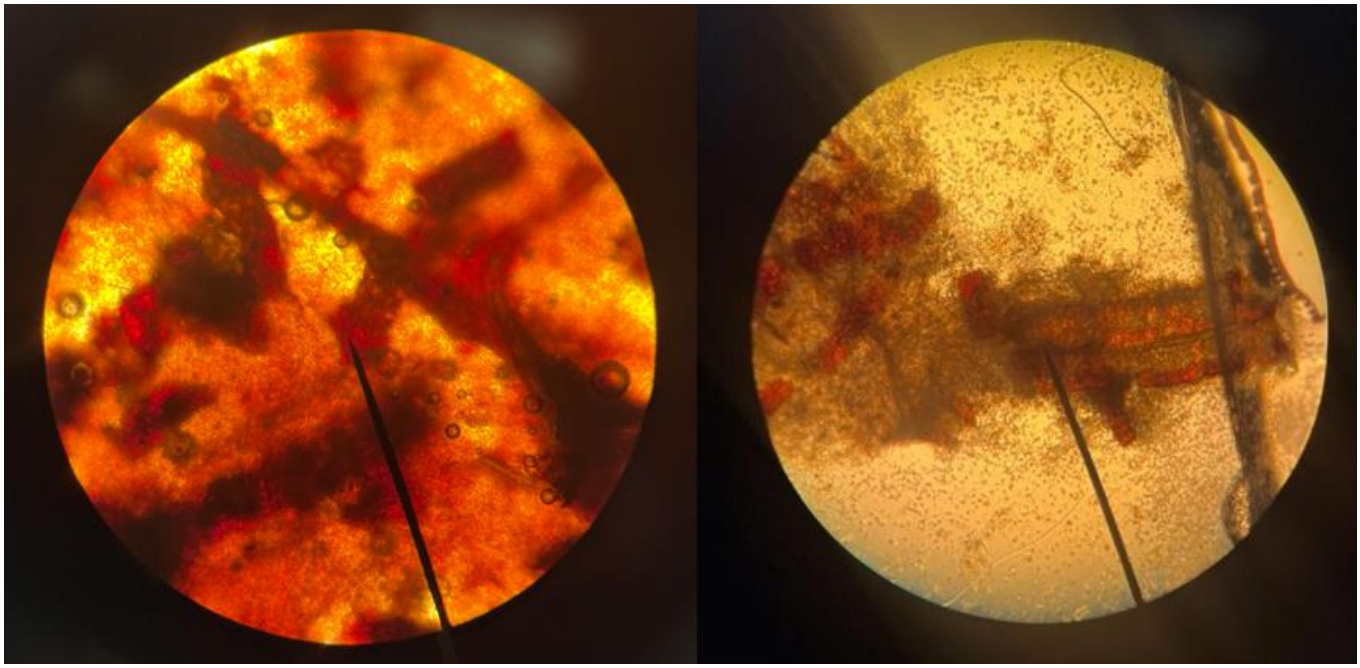

Figure 7. Microscopic View of Bioplastic.

Solubility Test

The solubility test was performed by placing samples of banana peel-starch composite bioplastic in various solvents. To assess chemical stability in different environments, the selected solvents were 5% distilled white vinegar, a diluted acetic acid (CH_3COOH) solution with an approximate pH of 2.4 as an acidic medium, tap water as a neutral medium, and nail polish remover containing acetone (CH_3COCH_3) as an organic solvent. Each batch was covered with polystyrene film to prevent evaporation and contamination, and changes were recorded after 24 hours.

Heat Resistance Test

To determine thermal stability, a sample of bioplastic on an aluminum sheet was placed on a hot plate. The heat setting was gradually increased every 10 minutes. Approximate temperatures were measured with a thermometer, and significant observations were recorded at temperatures below 50°C, between 70°C and 80°C, and between 90°C and 100°C.

Flexibility and Elongation Test

A strip of banana peel-starch composite bioplastic was measured and its initial length recorded. The strip was then stretched to its maximum capacity, and the final length was measured to evaluate the bioplastic's elongation. The flexibility test was conducted by bending and twisting a separate strip of bioplastic, and any visible damage was noted.

Results

Chemical Stability

The solubility of each sample differed depending on the solvent. In water, the bioplastic was completely insoluble. In an acidic solution such as 5% white vinegar, the bioplastic dissolved significantly over a period of 24 hours. In nail polish remover containing acetone, an organic solution, the sample was only partially soluble, having preserved most of its shape at the core while dissolving at the edges.

Thermal Stability

Hot Plate Setting	Level 2	Level 5	Level 8
Tempe-ratures	Below 50˚C	At 70-80˚C	At 90-100˚C
Obser-vation	No visible changes	Formation of surface bubbles	Visible deformation, significant darkening

Figure 8. The table represents the observed thermal resistance of banana peel bioplastic heated on a hot plate at varying temperatures for 10 minutes per setting.

Noticeable changes were observed in the bioplastic as the temperature increased. As shown in Figure 8, at temperatures below 50˚C, no changes in colour, texture, or shape were observed. Between 70°C and 80°C, bubbles began forming on the surface of the bioplastic. Near 100°C, the sample exhibited visible deformation as well as pronounced darkening.

Elongation and Flexibility

The banana peel bioplastic displayed limited elongation, breaking under minimal pulling force. However, it demonstrated significant flexibility, as it could be bent and twisted without visible breakage.

Discussion

Solubility Test

The bioplastic was cut into pieces and immersed for 24 hours in different solutions, such as water, white vinegar, and acetone. Solubility plays a crucial role in biomaterials for the making of bioplastics. Since the main components of banana peel-starch composite bioplastic are starch, plasticizers, cellulose fibers, and glycerol, they all interact differently with polar and organic solvents.

The sample was insoluble in water, demonstrating how the starch molecules hydrogen bond together, creating a semi-cross-linked structure that prevents the water from penetrating through. This is an important property because bioplastics that are dissolvable in water are not suitable for practical applications.

The sample was soluble in 5% white vinegar, as it significantly dissolved in it. Vinegar is an acidic aqueous solution containing acetic acid that weakens the hydrogen bonds between these starch molecules. It could also break down the pectin and starch in the banana peels, increasing their solubility.

The sample was partially soluble in acetone, an organic solvent, by only dissolving the edges of the bioplastic sample, while the inner part remained intact. This is most likely due to the glycerol molecules being more exposed and easily extracted by this solvent at the edges, while the inner part is less accessible. Acetone doesn't interact as strongly with starch and cellulose, which are hydrophilic polymers.

Heat Test

The heat test results illustrate that the banana peel-starch composite bioplastic has moderate thermal resistance and starts to degrade once the temperature increases.

Below 50°C, there were no visible changes observed, suggesting that the structure remained stable at low temperatures. This stability is due to hydrogen-bonded molecules. These molecular bonds were not disrupted enough to cause structural changes.

At 70°C - 80°C, the formation of surface bubbles was observed. As the temperature increases, some of the moisture is trapped within the bioplastic vaporizes, creating these bubbles on the surface. This indicates that the material is not fully heat-resistant, which is typical for starch-based bioplastics.

At 90–100°C, the sample showed visible deformation and darkening. This suggests that the heat weakened the intermolecular hydrogen bonds, causing the material to soften and lose its shape. This demonstrates that bioplastics have a lower thermal tolerance compared to conventional petroleum-based plastics, which are heat insulators and minimize heat transfer in various applications [7].

Flexibility Test

This low elongation and high flexibility of the bioplastic suggest that it may be suitable for practical applications that require bending, such as biodegradable films or flexible packaging, but may not be ideal for other applications that require high mechanical strength or stretching resistance.

Furthermore, a key challenge in producing bioplastics from banana peels is maintaining consistent product quality. Since banana peels differ naturally in chemical composition and moisture content, it is difficult to establish the ideal conditions for transforming them into plastic. To improve the extraction and production quality of banana-derived cellulose, researchers have found that many aspects must be controlled. For instance, higher cellulose crystallinity allows us to achieve a stronger and more ordered internal structure, enhancing bioplastic toughness. Also, alkaline treatment showed improved bonding with the material of the bioplastic, by getting rid of impurities like lignin and hemicellulose, making a more porous surface [8]. This can influence flexibility, mechanical strength, and even biodegradability. Moreover, two different samples were made, with different amounts of the used substances. The left sample shown in Figure 7 illustrates how the bioplastic made with no cornstarch and less glycerol looked under a microscope. It can be observed that the banana peels are closer to one another, reducing the flexibility of the sample. This sample was not flexible and felt mostly like paper. The right of Figure 7 shows the sample made with cornstarch and a higher amount of glycerol, where the sample had a more plastic feel to it. Therefore, it is important to optimize processing and pretreatment methods to synthesize more high-quality and reliable bioplastics. Note that bioplastic can also be made from other kinds of food waste, such as potato peels and orange peels [9].

Conclusion

This study successfully demonstrated the synthesis of bioplastics from banana peels, transforming food waste into a sustainable alternative to conventional plastics. Conventional plastics are used widely because of their low cost, water resistance, and availability, but they are made from fossil fuels, are non-biodegradable, and have led to severe environmental problems, including plastic pollution, loss of biodiversity, and increased greenhouse gas emissions contributing to global warming.

Banana peels provide an eco-friendly material for bioplastic production. In this study, banana peel paste was mixed with glycerol, NaOH, HCl, and cornstarch to form a bioplastic that was tested for solubility, thermal resistance, flexibility, and elongation to assess its properties. The bioplastic was water-resistant but soluble in acidic conditions, partially soluble in organic solvents, thermally stable at low temperatures, and flexible despite limited elongation. These results indicate that banana peel starch composite bioplastics have promising properties for applications such as biodegradable films and flexible packaging, while remaining environmentally safe and degradable.

Overall, the study shows that banana peel starch composite bioplastics can reduce reliance on conventional plastics, decrease environmental pollution, and valorize food waste. This approach offers a practical and sustainable solution to the global challenges of plastic pollution and food waste management.

References

[1] Bucher, S. (2022). The spiral of plastic pollution: a compensatory urge from the collective unconscious for an ecological-psychological transformation of civilization. *Journal of Analytical Psychology*, *67*(5), 1386–1409. https://doi-org.dawsoncollege.idm.oclc.org/10.1111/1468-5922.12861

[2] Padilla-Vasquez, D. (2024, May 1). Protect our planet from plastic pollution: 5 things to know. UN Foundation. https://unfoundation.org/blog/post/protect-our-planet-from-plastic-pollution-5-things-to-know/

[3] Agbedahin, A. V., & Agbedahin, K. (2019). Food Waste in University Spaces. *Peace Review*, *31*(4), 532–538. https://doi-org.dawsoncollege.idm.oclc.org/10.1080/10402659.2019.1800944

[4] Ravi, I., & Mustaffa, M. M. (2013). Starch and amylose variability in banana cultivars. Indian Journal

of Plant Physiology, 18(1), 83–87. https://doi.org/10.1007/s40502-013-0014-2

[5] Talukdar, N., Boro, R. C., Purkayastha, M. D., Nath, T., Rathi, S., & Sarmah, K. (2025). Exploring banana peels as a renewable source for bioplastic development. International Journal of Advanced Biochemistry Research, 9(1), 22–30. https://doi.org/10.33545/26174693.2025.v9.i1a.3407

[6] Ghataty, D. S., Amer, R. I., Wasfi, R., & Shamma, R. N. (2022). Novel linezolid loaded bio-composite films as dressings for effective wound healing: experimental design, development, optimization, and antimicrobial activity. *Drug Delivery*, *29*(1), 3168–3185. https://doi-org.dawsoncollege.idm.oclc.org/10.1080/10717544.2022.2127

[7] Thermal Conductivity of Polymers and Plastics. (n.d.). Matmake. Retrieved February 22, 2026, from https://matmake.com/properties/thermal-conductivity-of-polymers-and-plastics.html

[8] EngiSphere Research Editors. (2025, November 1). *From banana waste to bioplastics: How cellulose from discarded banana stems could revolutionize the future of sustainable biopolymers*. EngiSphere. https://engisphere.com/banana-waste-to-bioplastics-biopolymers/

[9] Ahn, S. (2025). *Bioplastics from food by-products*. In *Bioplastics within the circular bioeconomy*. IntechOpen. https://doi.org/10.5772/intechopen.1007357

Impact of Coefficient of Kinetic Friction on the Distances Traveled by a Coin Stack

Lina Berima, Vanessa Charles

Abstract – This experiment investigates the relationship between the ratio of distances traveled by stacked coins upon an inflicted uniform horizontal push and the coefficient of kinetic friction of the coins in contact with different surfaces.

Introduction

The behaviour of a stack of coins when treated with an external force provides an opportunity to study friction and motion in a multi-body system. The objective of this experiment is to calculate the ratio of the distances travelled between the first and second coin, starting from the bottom, and the second and third coins in a stack of three identical coins, following a uniform horizontal push. In fact, we seek to study how these ratios are influenced by the coefficient of kinetic friction, which will differ across various surface types: soft wood, rough wood and standard bathtub enclosure.

Our hypothesis is that the ratio of the distances travelled of coin 1 in relation to coin 2 and the distances travelled of coin 2 in relation to coin 3 will be inversely proportional to the coefficient of friction between the coin and the surface.

The coefficient of kinetic friction is known as the ratio of the kinetic friction force to the normal force. It varies due to the nature of both surfaces when they rub against each other [1].

In order to calculate the coefficient of kinetic friction of the chosen surface, we use Newton's second law:

$$F_{net} = ma \qquad (1)$$

Where F_{net} , m and a respectively correspond to the net force in newtons, which would be the kinetic friction force between the coin and the chosen surface in our case, the mass of the coin in kilograms and the acceleration of the coin in meters per second squared [2]. Therefore, when a coin slides on a surface until it's at rest, the value of the kinetic friction force can be calculated using its mass and acceleration.

Then, we use the formula of the kinetic friction to find the coefficient of kinetic friction:

$$F_k = \mu_k n \qquad (2)$$

Where F_k, μ_k and n respectively correspond to the kinetic friction force in newtons, the coefficient of kinetic friction, and the normal force in newtons [3].

Experimental Setup

The raw data in this experiment corresponds to the acceleration of a coin on a surface as well as the distance between coin 1 in relation to coin 2 and the distance between coin 2 in relation to coin 3 from the launch of the stacked pile of coins.

How to Find the Acceleration of One Coin

To find the acceleration of a single coin on a horizontal surface, we recorded a video where one was being pushed by a wooden plate on a chosen surface with a ruler as a reference point. This video was then imported on a software called *Tracker*, which enabled us to track the movement of our coin [4] (Refer to Figure 2).

After uploading the recording, we set up an axis on the coin to follow its movement at every moment. Furthermore, we used the *calibration stick* tool to create a reference frame on the ruler, measuring it from the position of the coin where the wooden plate wasn't pushing it anymore (i.e. wasn't in contact with it) to the end of the ruler. Then, using the software, we tracked the position of the coin from that moment until the coin stopped sliding.

Tracker generated a graph of velocity versus time (refer to Figure 1.) as well as its equation in a linear format ($y = ax + b$). It is indeed a linear relationship because the acceleration of the coin is constant. Finally, by deriving it, we found the value of a as our acceleration and repeated the process twenty-five times on each different surface.

How to Find the Distance Between Each Stacked Coin

To find the distances between the coins, we applied a uniform push using a wooden plate to a stack of three coins that were identified with colors (the one on the bottom was red (1), the one in the middle blue (2), the one above, green (3) (refer to Figure 3).

Then, when they all stopped sliding, we measured the distance between each coin, specifically 1 to 2 and 2 to 3, by placing a ruler, ensuring that both ends (i.e. the first end starting at the zero millimeter mark) were in the middle of each coin.

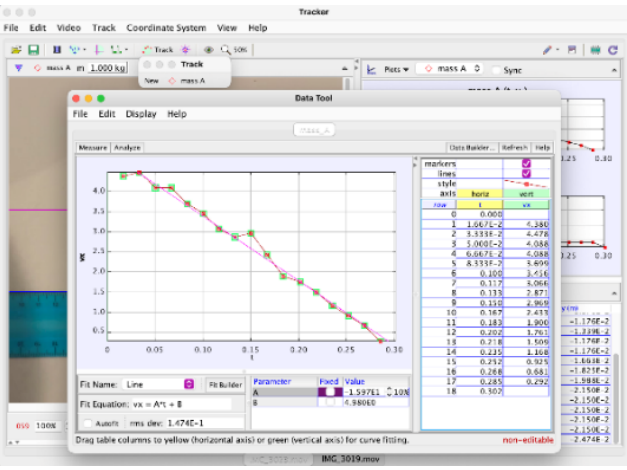

Figure 1. Velocity vs time graph generated on Tracker.

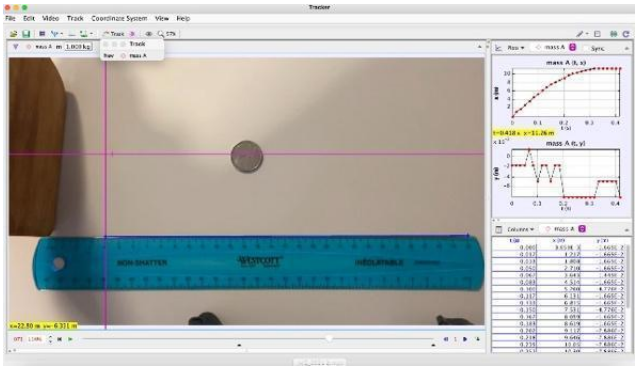

Figure 2. Preview of the software Tracker with a video template and frame of reference.

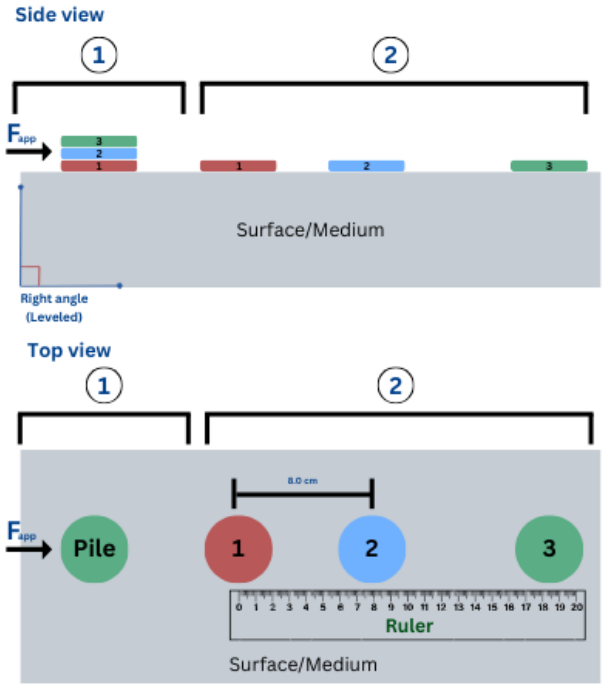

Figure 3. Illustration of the stack of coins sliding and the setup used to measure the distance.

Data and Analysis

During the experiment, we recorded twenty-five times the acceleration of one coin on 3 different surfaces using the same coin as the ones that were stacked. We then calculated the coefficient of kinetic friction on each medium with the help of the data collected.

We also recorded the distance between coins 1 and 2, and the distance between coins 2 and 3 when the 3 stacked coins were uniformly pushed on one surface. We did this process twenty-five times for each surface. Then, to find

the ratio of the coins, we divided the distance between coins 1 and 2 by the distance between coins 2 to 3.

Coefficient of Kinetic Friction

Table 1 represents all the data collected on the first surface which was a soft wooden desk.

Trial	α (m/s²) ±0.12	μ_k ±0.013
1	-1.66	0.169
2	-1.69	0.172
3	-1.69	0.172
4	-1.87	0.191
5	-1.75	0.179
6	-1.75	0.179
7	-1.88	0.192
8	-3.19	0.326
9	-2.08	0.212
10	-2.03	0.207
11	-1.82	0.186
12	-1.91	0.195
13	-1.89	0.193
14	-1.68	0.171
15	-1.72	0.176
16	-2.05	0.209
17	-1.68	0.171
18	-1.82	0.186
19	-2.24	0.229
20	-2.10	0.214
21	-1.83	0.187
22	-2.06	0.210
23	-2.10	0.214
24	-1.77	0.181
25	-1.82	0.186
Average:	-1.92	0.196

*Table 1. Acceleration (**a**) in m/s² and coefficient of kinetic friction (μ_k) of a coin on a soft wood surface with uncertainties included.*

The same tables for the other two different surfaces, rough wood and standard bathtub enclosure, can be found in the Appendix.

Then, to find the coefficient of kinetic friction, we analyzed the forces acting on the coin during each of our trials. As mentioned earlier, we started by pushing a coin on a chosen surface until it slid, making sure the object that caused it to move was no longer physically in contact with it.

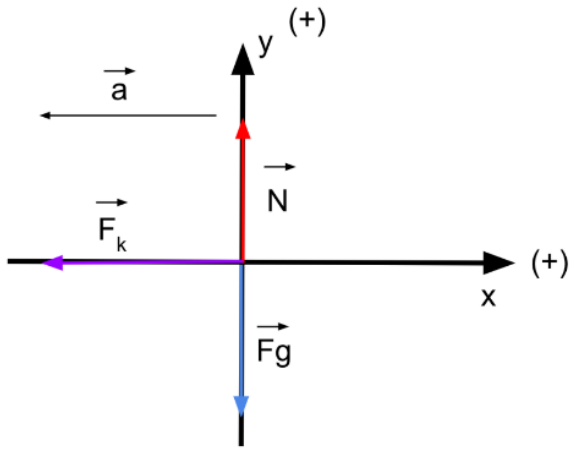

Figure 4. Free body diagram of a coin sliding on a surface once the object that caused it to move is no longer in contact with it.

At that moment, we could conclude that the only forces acting on the coin were the kinetic friction, which causes the coin to eventually come to a stop, the normal force, and the force due to gravity, which cancel each other out due to them having the same magnitude but opposite signs, and being on the same axis on a flat surface (Refer to Figure 4).

This means that the sum of forces on the x-axis, which only contains the kinetic friction force, according to Newton's second law, will be equal to the product of the mass and the acceleration of the coin. To find the coefficient of kinetic friction, we take the absolute value (since the coefficient can't be lower than zero) of the product of the mass and acceleration divided by the normal force, which is equal to the gravitational pull of the Earth times the mass of the coin in kilograms. We can then find that the coefficient of kinetic friction between a horizontal surface and a sliding coin is:

$$\mu_k = \left|\frac{a}{g}\right| \qquad (3)$$

where μ_k , a and g respectively correspond to the coefficient of kinetic friction, the acceleration of the coin in meters per second squared, and the acceleration due to Earth's gravity. This equation represents the kinetic friction force divided by the normal force. Therefore, we only need to find the acceleration of the coin and then divide it by the gravitational pull of the earth, which is 9.80 m/s² [5].

Uncertainties on the Coefficient of Kinetic Friction

To find the uncertainty of the coefficient, we started by calculating the average, also known as the mean, of the acceleration points we collected. After, we calculated their standard deviation with the following formula,

$$s_x = \sqrt{\frac{\sum(x - \bar{x})^2}{(n-1)}} \quad (5)$$

given by the Excel function "=STDEV.S" to see the likelihood of the next measurement in relation to the mean [6]. Then, we calculated the standard deviation of the mean, which is equal to the standard deviation divided by the square root of the number of values collected, which was 25 in our case, with the formula

$$s_{\bar{x}} = \frac{s_x}{\sqrt{n}} \quad (6)$$

To find the uncertainty of the coefficient, we started by calculating the average, also known as the mean, of the acceleration points we collected. After, we calculated their standard deviation of the mean with equation (6) [7]. By multiplying the standard deviation of the mean by two, we found the uncertainty of the acceleration for a 95% confidence interval which was ±0.12 m/s² for soft wood; ±0.2 m/s² for rough wood and ±0.16 m/s² for standard bathtub enclosure.

Something important to address is the systematic uncertainty on the acceleration. Due to the way the data points were collected, the uncertainty corresponds to the change brought by every different trial and video, meaning it's not necessarily the way the application *Tracker* itself measured. We decided not to take it into account since the change wouldn't make any significant difference based on our inspection. Also, the reference frame on *Tracker* could've been a source of systematic uncertainty but is negligible.

After finding the uncertainty of the acceleration, we applied the propagation of uncertainties formula to find the absolute uncertainty on the coefficient of kinetic friction. We will use equation (4) to do so. As it is a division, we used the following formula to find the relative uncertainty:

$$\frac{\delta a}{|a|} + \frac{\delta g}{|g|} \quad (7)$$

where δa and δg are respectively equal to the uncertainties on the acceleration, and the uncertainties on the acceleration due to gravity; a and g are respectively equal to the average acceleration on one surface, and the acceleration due to gravity. Also, note that we assumed that the uncertainty on the acceleration due to gravity was equal to ±0.01 m/s² based on standard ruling [8]. Ultimately, we multiplied the value obtained by the average μ_k which resulted in the absolute uncertainty on the coefficient of kinetic friction which was, respectively for each surface, ±0.013 for soft wood; ±0.02 for rough wood and ±0.02 for standard bathtub enclosure.

Soft Wood μ_k **±0.013**	**Rough Wood** μ_k **±0.02**	**Bathtub Enclosure** μ_k **±0.02**
0.196	0.25	0.34

Table 2: Coefficient of kinetic friction (μ_k) as well as their uncertainty for the three surfaces used during the experiment.

Ratios of Distances Travelled

Table 2 shows the 25 different values of both distances recorded on the soft wood surface which corresponds to a desk in that case, and the ratio of these distances.

Trial	$d_{1\ to\ 2}$ (m) ±0.001	$d_{2\ to\ 3}$ (m) ±0.001	Ratio of Distances ±0.09
1	0.055	0.060	0.92
2	0.060	0.080	0.75
3	0.075	0.070	1.07
4	0.085	0.110	0.77
5	0.060	0.135	0.44
6	0.085	0.147	0.58
7	0.101	0.111	0.91
8	0.080	0.115	0.70
9	0.072	0.072	1.00
10	0.040	0.066	0.61
11	0.084	0.070	1.20
12	0.067	0.070	0.96
13	0.074	0.103	0.72
14	0.077	0.060	1.28
15	0.083	0.125	0.66
16	0.059	0.100	0.59
17	0.075	0.090	0.83
18	0.110	0.095	1.16
19	0.065	0.095	0.68
20	0.075	0.100	0.75
21	0.080	0.095	0.84
22	0.070	0.112	0.63
23	0.086	0.086	1.00
24	0.080	0.070	1.14
25	0.080	0.110	0.73
Average:	0.075	0.094	0.84

Table 3: Distance between coins 1 and 2 ($d_{1\ to\ 2}$), distance between coins 2 and 3 ($d_{2\ to\ 3}$), and the ratio of the distance of each trial after pushing horizontally and uniformly the 3 stacked coins on the soft wood surface.

The same tables for the two other different surfaces, rough wood and standard bathtub enclosure, can be found in the Appendix section.

Uncertainties on the Ratio of the Distance Travelled Between the Coins

The uncertainty for the distances between coins 1 and 2 and distances between coins 2 and 3 corresponds to the smallest value on the ruler used, which was 0.001 meters. It is also equal to the systematic uncertainty. The way we collected this data makes us unable to use the standard deviation formula since the data points were not continuous. We then propagated these uncertainties on the ratio with the help of the formula

$$\frac{\delta d1}{|d1|} + \frac{\delta d2}{|d2|} \qquad (7)$$

where $d1$ is equal to the average distance between coin 1 and 2; $d2$ is equal to the average distance between coin 2 and 3, and $\delta d1$ and $\delta d2$ represent the uncertainty on each, to determine the relative uncertainty. To find the absolute uncertainty, hence the systematic uncertainty, we multiplied the previous value by the average ratio [9].

Next, to find the statistical uncertainty on the ratio, we used the same method previously shown when finding the statistical uncertainty on the acceleration. We calculated the mean and then determined the standard deviation with equation (5) and found the standard deviation of the mean using equation (6). By multiplying the standard deviation of the mean by two, we found the statistical uncertainty of the ratio.

Finally, we found the complete uncertainty by using the following formula

$$\delta A = \sqrt{\delta t^2 + \delta y^2} \qquad (8)$$

where δA is the total uncertainty, δt is the statistical uncertainty, and δA is the systematic uncertainty [10].

We determined that, for each respective surface, the uncertainty on the ratio was ±0.09 m for soft wood, ±0.06 m for rough wood, and ±0.04 m for standard bathtub enclosure.

After gathering our data and doing all the necessary calculations, we plotted a graph to determine the relationship between the ratios and coefficients of friction of each respective surface. We obtained the following graph consisting of 3 data points:

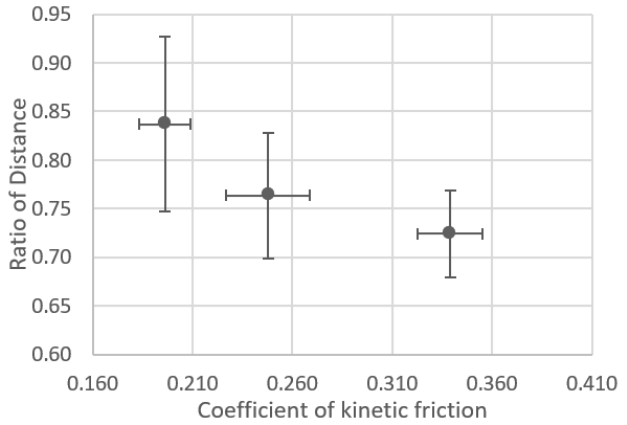

Figure 4. The ratio of distances with respect to the coefficient of kinetic friction with error bars included for the three surfaces.

Conclusion and Discussion

In conclusion, when analyzing the graph, we can see that the average data points correspond to the following relationship: when the coefficient of kinetic friction increases, the ratio of distance decreases. However, we are unable to precisely determine the nature of the relationship, meaning if it is linear, inversely proportional, etc. due to the lack of data points. Therefore, we cannot fully state that our hypothesis was correct or wrong and would need more data points to have more accuracy. Furthermore, the number of data points was not the only reason we were unable to state that our hypothesis was correct. Indeed, when taking into account the uncertainties, the relationship previously stated isn't accurate anymore. In fact, the points can align in a constant fashion or even be scattered randomly on the intervals created by the uncertainties. Hence, we cannot state that the data completely corresponds to the hypothesis because of the lack of precision and correlation. Due to the error bars, notably on the ratio of distances, there is a big range of data possible for each point which makes it highly possible that the three points follow entirely different relationships and trends.

Therefore, it is still possible that our hypothesis is correct, which is that the ratio of the distance of the coins 1 to 2 and the distance of coins 2 to 3 will be inversely proportional to the coefficient of friction between a coin and a surface. It is also possible that the relationship studied is different and follows another trendline, such as linear one or even that there is no relationship to begin with. Therefore, we cannot say anything about the nature of that relationship for now.

During the experiment, there were many external sources of error or measuring methods that we didn't take into account and that could have influenced our results significantly.

In fact, one of the limitations we encountered in the experiment was that we had to manually track the position of the coin on the software *Tracker*. Despite tracking it multiple times for many frames, the fact that it was done manually removed precision in the tracking and therefore influenced all the values generated based on it. It's probable that some acceleration values during a few trials were not accurate, influencing the average acceleration found for the surfaces which would in turn change the value of the kinetic friction and then the coefficient of kinetic friction. Furthermore, this inaccuracy could've also influenced the statistical uncertainty on the acceleration, as the data could've become more scattered, increasing the standard deviation, hence the statistical uncertainty

In addition, when measuring the distances by pushing a stack of 3 coins, the patterns were somewhat irregular, as the distance between 1 and 2 was sometimes larger or smaller than the distance between 2 and 3, and vice-versa. These significantly different distances caused the ratios to be extremely different from one another, scattering their values even more, hence the increased standard deviation on the ratio and, consequently, the statistical uncertainty on the ratio. We are not certain what caused these irregularities related to the distance since we made sure to push the stack of coins uniformly with a wooden plank. However, we think that one of the main reasons could have been that since we actively pushed said plank while holding its edge with our fingers, it is possible that the force wasn't uniformly distributed on said object and by default, on the coins. We held the plank from its top, which could've created a slight angle, either forward or backward, on the vertical axis during the motion. Therefore, depending on the orientation of the plank, the coins on top or on the bottom could've received more force or less force, hence sliding further or lesser.

Another relevant point to address is the initial assumption that the velocity wasn't going to affect the ratio. Under

normal circumstances, meaning when the coins are pushed by a force applied uniformly on the stack, that assumption could be true since the initial velocity would technically be the same for all the coins, making them slide in a continuous manner, meaning the ratios would be somewhat the same and its uncertainty lower. However, as mentioned earlier, in our case, the coins could've not been pushed uniformly, which could've caused the initial velocity to differ per coin and make our distances discontinuous, meaning the values of the ratios were extremely different, making their values more scattered and increasing the standard deviation on the ratio, hence the statistical uncertainty. This would explain why we got such high uncertainties that made us unable to determine any concrete relationship with the ratio.

Acknowledgements

We would like to express our gratitude to our Mechanics instructor, Jean-François Brière, for his guidance and support throughout this project. His feedback was essential in helping us understand many aspects of our experiment and finish our paper.

Appendix

Trial	α (m/s²) ±0.2	μ_k ±0.02
1	-1.7	0.17
2	-2.0	0.20
3	-2.2	0.22
4	-2.2	0.22
5	-2.2	0.22
6	-2.3	0.24
7	-2.2	0.22
8	-4.6	0.47
9	-2.3	0.24
10	-2.3	0.23
11	-2.0	0.21
12	-2.4	0.25
13	-2.5	0.26
14	-2.6	0.27
15	-2.4	0.24
16	-2.5	0.25
17	-2.3	0.23
18	-2.4	0.25
19	-2.4	0.25
20	-2.4	0.24
21	-2.6	0.26
22	-2.6	0.26
23	-2.5	0.25
24	-2.4	0.25
25	-2.8	0.28
Average:	-2.4	0.25

*Table 4. Acceleration **(α)** in m/s² and coefficient of kinetic friction (μ_k) of a coin on a rough wood (floor) surface.*

Trial	α (m/s²) ±0.16	μ_k ±0.02
1	-2.69	0.27
2	-2.88	0.29
3	-2.81	0.29
4	-3.10	0.32
5	-2.92	0.30
6	-3.07	0.31
7	-3.27	0.33
8	-4.57	0.47
9	-3.15	0.32
10	-3.34	0.34
11	-3.17	0.32
12	-2.99	0.31
13	-3.85	0.39
14	-3.19	0.33
15	-3.28	0.33
16	-3.62	0.37
17	-3.55	0.36
18	-3.15	0.32
19	-3.50	0.36
20	-3.57	0.36
21	-3.52	0.36
22	-3.22	0.33
23	-3.61	0.37
24	-3.51	0.36
25	-3.52	0.36
Average:	-3.32	0.34

*Table 5. Acceleration **(α)** in m/s² and coefficient of kinetic friction (μ_k) of a coin on a rough wood (floor) surface*

Trial	$d_{1\ to\ 2}$ (m) ±0.001	$d_{2\ to\ 3}$ (m) ±0.001	Ratio Distance ±0.06
1	0.060	0.075	0.80
2	0.060	0.050	1.20
3	0.065	0.100	0.65
4	0.057	0.065	0.88
5	0.060	0.117	0.51
6	0.085	0.095	0.89
7	0.070	0.087	0.80
8	0.078	0.095	0.82
9	0.102	0.170	0.60
10	0.045	0.079	0.57
11	0.084	0.094	0.89
12	0.070	0.075	0.93
13	0.070	0.098	0.71
14	0.087	0.137	0.64
15	0.090	0.120	0.75
16	0.075	0.100	0.75
17	0.067	0.080	0.84
18	0.070	0.095	0.74
19	0.080	0.120	0.67
20	0.080	0.115	0.70
21	0.117	0.217	0.54
22	0.066	0.095	0.69
23	0.120	0.117	1.03
24	0.055	0.075	0.73
25	0.060	0.080	0.75
Average:	0.075	0.102	0.76

Table 6. Distance between coin 1 and 2 ($d_{1\ to\ 2}$), distance between coin 2 and 3 ($d_{2\ to\ 3}$), and the ratio of the distance of each trial of pushing the 3 coins uniformly on the rough wood (floor) surface.

Trial	$d_{1\ to\ 2}$ (m) ±0.001	$d_{2\ to\ 3}$ (m) ±0.001	Ratio Distances ±0.04
1	0.045	0.060	0.75
2	0.045	0.078	0.58
3	0.055	0.070	0.79
4	0.050	0.100	0.50
5	0.075	0.087	0.86
6	0.082	0.104	0.79
7	0.048	0.088	0.55
8	0.072	0.087	0.83
9	0.053	0.076	0.70
10	0.069	0.085	0.81
11	0.085	0.110	0.77
12	0.070	0.110	0.64
13	0.075	0.124	0.60
14	0.064	0.093	0.69
15	0.066	0.100	0.66
16	0.065	0.090	0.72
17	0.065	0.086	0.76
18	0.089	0.099	0.90
19	0.085	0.101	0.84
20	0.062	0.101	0.61
21	0.076	0.102	0.75
22	0.068	0.085	0.80
23	0.089	0.125	0.71
24	0.065	0.092	0.71
25	0.069	0.086	0.80
Average:	0.067	0.094	0.72

Table 7. Distance between coin 1 and 2 ($d_{1\ to\ 2}$), distance between coin 2 and 3 ($d_{2\ to\ 3}$), and the ratio of the distance of each trial of pushing the 3 coins uniformly on the standard bathtub enclosure surface.

References

[1] “Kinetic Friction: Definition, Relationship & Formulas | Vaia.” Vaia, 2019, www.vaia.com/en-us/explanations/physics/translational-dynamics/kinetic-friction/.

[2] Hall, Nancy. “Newton’s Laws of Motion.” NASA, 27 June 2024, https://www1.grc.nasa.gov/beginners-guide-to-aeronautics/newtons-laws-of-motion/#newtons-third-law-action-reaction.

[3] “6.4: Friction (Part 1).” OpenStax, https://phys.libretexts.org/Workbench/PH_245_Textbook_V2/06%3A_Applications_of_Newton's_Laws/6.04%3A_Friction_(Part_1).

[4] Brown, Douglas et al. Tracker. Version 6, Open Source Physics, 2024.

[5] Dasilva, Marcello and Nancy Hall. “Weight Equation.” NASA, 23 Nov. 2023, https://www1.grc.nasa.gov/beginners-guide-to-aeronautics/weight-equation-2/.

[6] Excel. Version 16.88 (24081116), Microsoft, 13 Aug. 2024.

[7] Kenton, Will. “Standard Error (SE) Definition: Standard Deviation in Statistics Explained.” Investopedia, 9 Aug. 2024, https://www.investopedia.com/terms/s/standard-error.asp.

[8] Brière, Jean-François. 203-NYA-05 at Dawson College, November 2023, Montreal, QC. Lecture.

[9] Advanced Instructional Systems, Inc. and Peter Bohacek. “Uncertainty Help.” Physics Explorations with Direct Measurement Videos - Uncertainty Help – 1, 2013, https://www.webassign.net/bohphysvl1/uncertainty.pdf.

[10] Holden, Micheal. “ME 360 10 02 Systematic and Random gives Total Uncertainty.” Youtube, uploaded by Professor Holden, 31 Oct. 2021, https://www.youtube.com/watch?v=mmHIGHwbKG0.

Experimental Verification of the Python Simulation of the Low-Pass Frequency Filter by Using the PASCO Capstone Interface

Vladimir Feshchenko, Eric Robert Desautels, Nobert Kristof, Édouard Bélair

Abstract – In this paper, we presented the results of the comparative analysis of the application of the Low-Pass Frequency (LPF) Butterworth filter to the non-sinusoidal signals (in our case, a square waveform) and its Python simulation, which included using Python's libraries NumPy and Matplotlib in Visual Studio Code (VSC) environment. The experimental part was implemented by the PASCO Capstone interface with embedded FFT. Both theoretical and experimental results matched each other.

Introduction

The multifunctional PASCO Capstone interface provides not only experimental measurements but also interpretation (analysis) of the results [1]. In our opinion, it could become a link connecting the theoretical methods of signal analysis and their experimental verification. In this paper, we made the first attempt at such an approach, that is, we used FFT and computer simulation on one hand, and PASCO Capstone on the other to examine the behavior of a passive low-pass filter using the PASCO 850 Universal Interface as the waveform source and data-acquisition system. This paper is written as a lab-style guide so students can reproduce both the computer simulation and the filter's frequency-dependent response.

Theoretical Background for LPFs

A low-pass filter allows low-frequency signals to pass while reducing higher-frequency harmonics. A square-wave input is useful for this experiment because it contains a series of odd harmonics, making attenuation easy to observe. A second-order LPF signifies that any voltage or current in the circuit can be described by a second-order differential equation. This forms a harmonic oscillator, such as an LC circuit. The main difference is that only low frequencies will pass through the load resistor (which is in parallel to C), since, for high frequencies, a branch with the capacitor acts as a short circuit. A more detailed analysis is presented in Appendix 1.

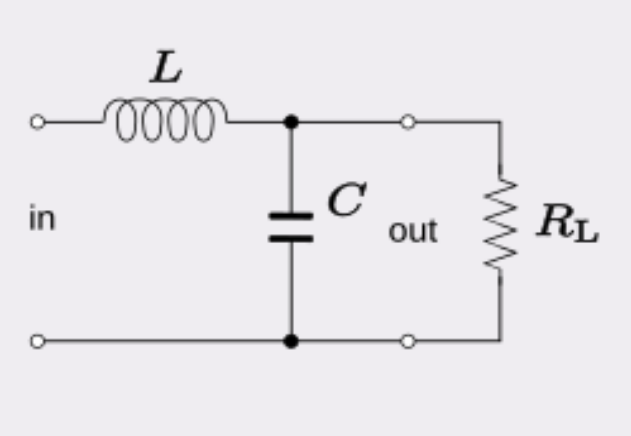

Figure 1: RLC passive low-pass filter of second order.

Python Simulation of LPF

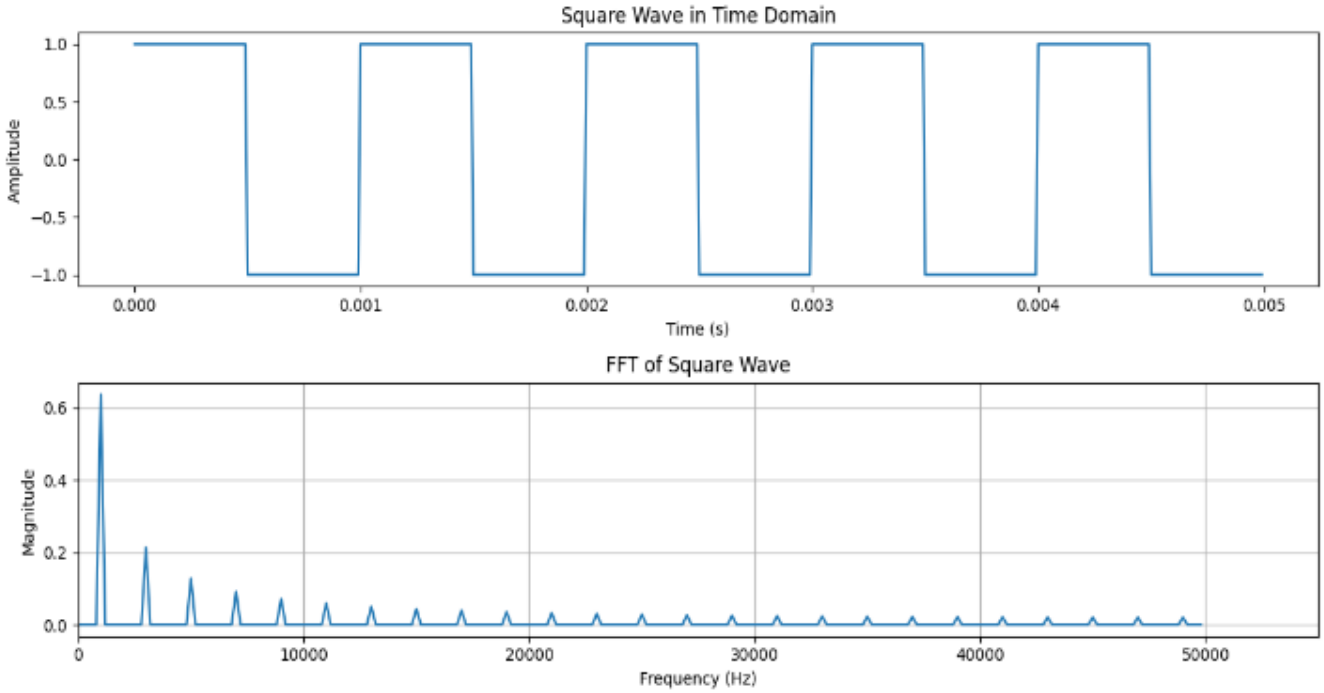

Figure 2: Square wave signal in both time and frequency domains (the frequency of the square wave is 1kHz, which is also the cutoff frequency of the LPF). (see Appendix 2).

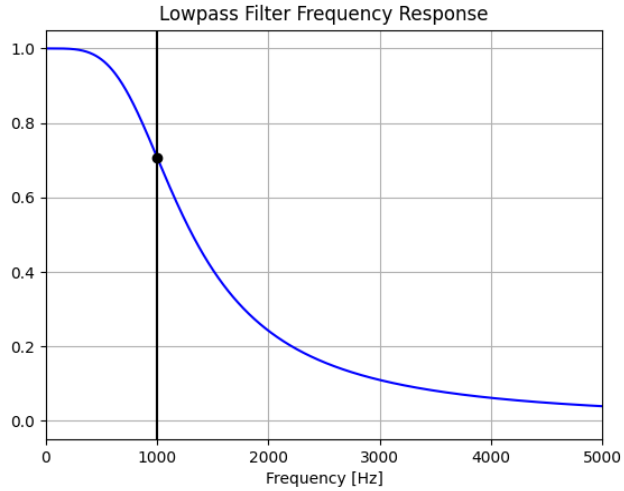

Figure 3. LPF response with the cutoff frequency of approximately 1KHz. [2,3] (see Appendix 3).

PASCO 850 Interface Overview

The PASCO 850 Universal Interface serves as both the function generator and the measurement system for this experiment. Its key features relevant to this lab include:

• **Output 2** — a ±10 V BNC waveform output capable of generating square, sine, triangle, and ramp signals.

• **Fine frequency control** resolution down to 0.001 Hz.

• **Synchronized acquisition** waveform generation and voltage sensing that share the same timing system.

• **Analog Inputs** compatible with PASCO voltage sensors for capturing low-level circuit behavior.

The 850 Interface replaces a traditional oscilloscope and function generator, making the setup simpler and ensuring measurements remain time-aligned. Because the generator and sensor operate through the same hardware, students can avoid phase differences that normally occur when using separate instruments.

LPF Experiment

Circuit Setup

• Measure the output across the capacitor.

• Connect the resistor in parallel with the capacitor.

1. Build the RLC low-pass filter on the breadboard:

2. Connect Output 2 of the PASCO 850 to the input of the RC circuit.

3. Connect the PASCO voltage sensor across the capacitor (filter output).

4. Plug the voltage sensor into an analog input port on the 850 Interface.

5. Open PASCO Capstone and verify that the interface and sensor are detected.

Procedure

1. In Capstone, open the signal generator controls for **Output 2**.

2. Set the waveform to **Square Wave**.

3. Start with a low frequency (e.g., 50–100 Hz) and amplitude of about ±5 V.

4. Enable data recording and observe both the input and output waveforms.

5. Use the FFT tool to view the harmonic content of the output.

6. Increase the frequency gradually. Watch how the capacitor output becomes smoother and how higher harmonics weaken.

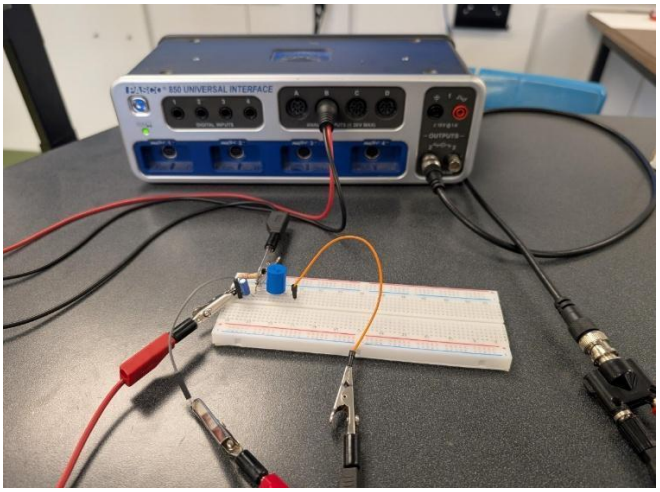

Figure 4: PASCO Capstone interface with LPF.

Conclusion

This experiment highlights the benefit of using the PASCO 850 Interface for circuit studies. Because the same unit generates the driving waveform and measures the output signal, timing is consistent, and data collection is simplified. Capstone's real-time FFT and waveform views make it straightforward for students to interpret the filter's behaviour without needing stand-alone oscilloscopes or frequency analyzers. The PASCO system effectively streamlines the learning process while maintaining accurate measurements.

Experimental Results and Discussion

At low frequencies, the output closely follows the sinusoidal wave. The observed behaviour matches the theoretical low-pass response curve.

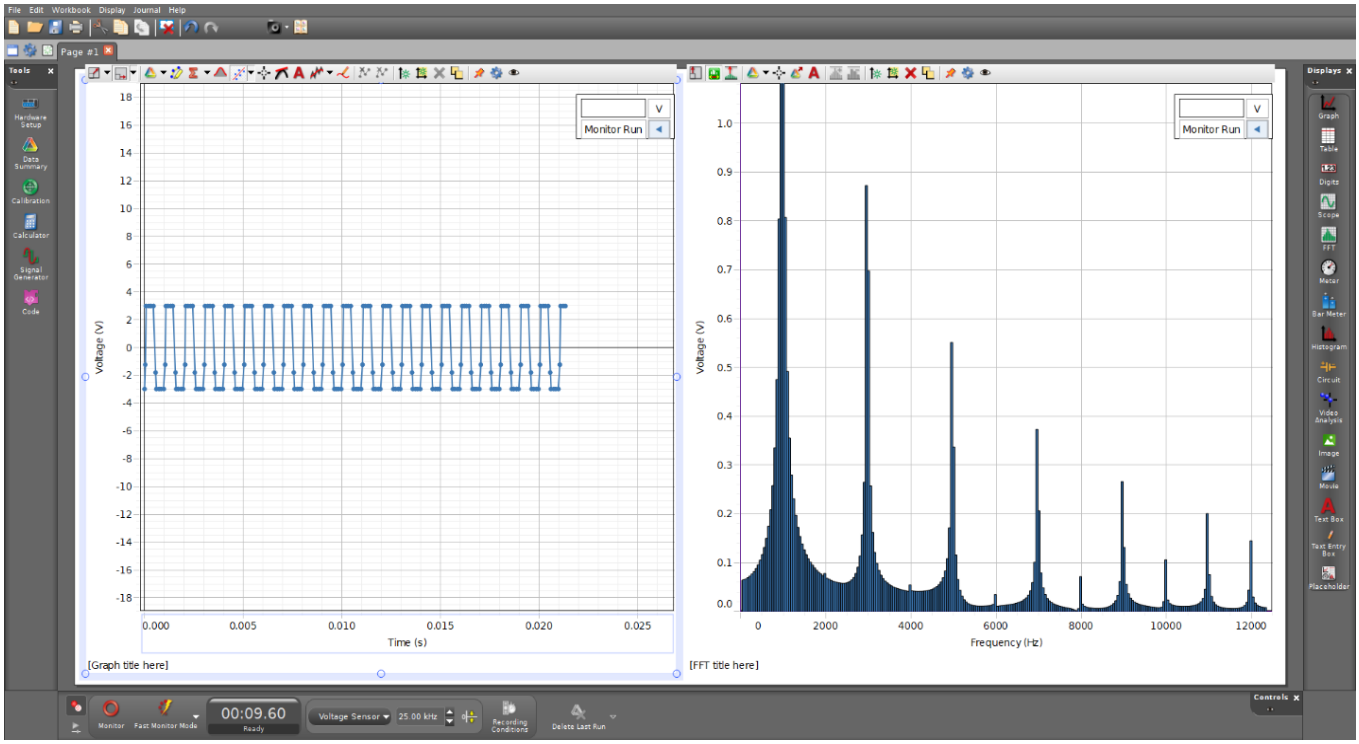

Figure 5: Input square wave signal and its FFT spectrum.

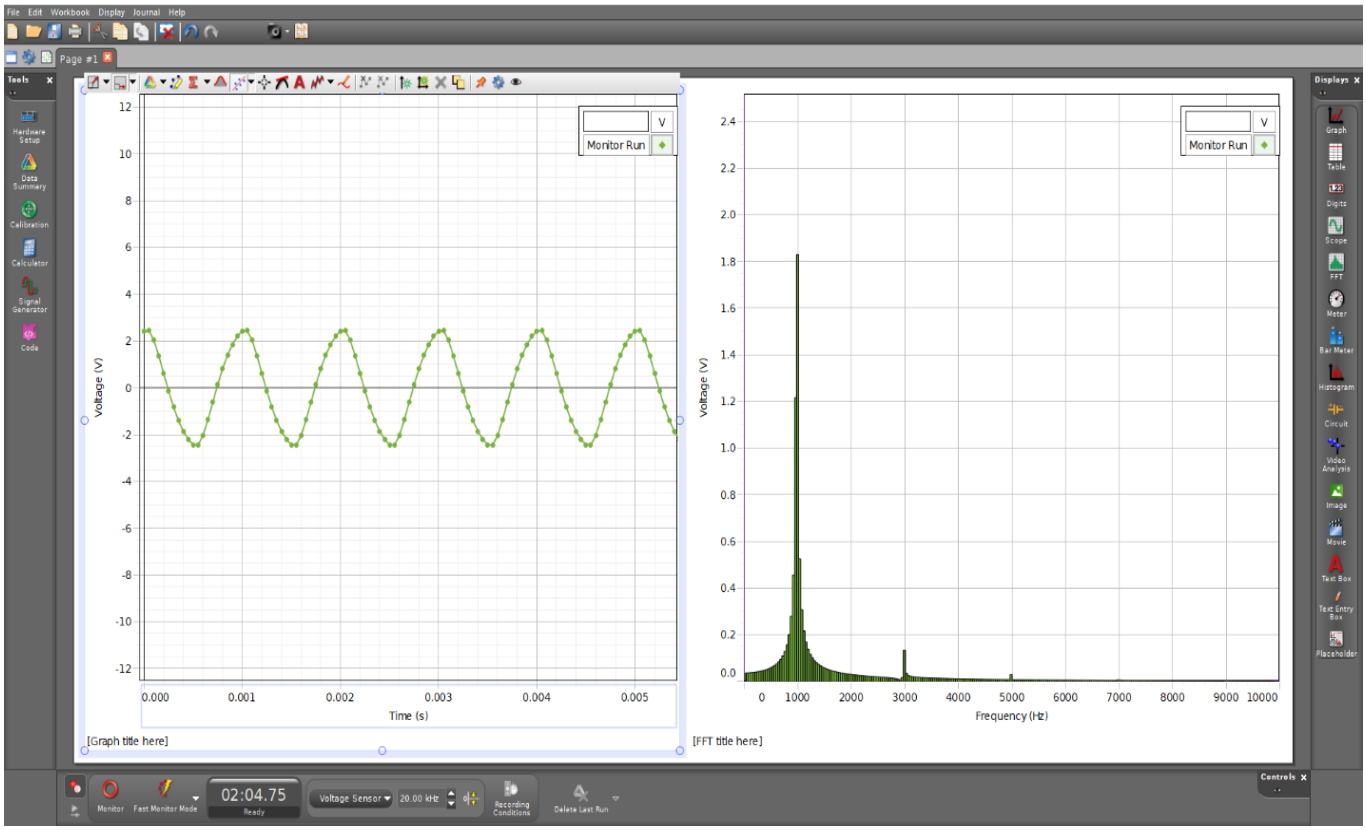

Figure 6: Output graph after LFP with almost one frequency (1kHz).

Reference

[1] PASCO Scientific, *850 Universal Interface (UI-5000) Product Guide*, Document 012-12355C.

[2] Shivkumar V.I. (2020) Digital Filter Design using Python for Power Engineering Applications, An Open Source Guide (pp.149-185), https://doi.org/10.1007/978-3-030-61860-57

[3] Navid F.R. (2021). Design, Implementation, Comparison, and Performance analysis between Analog Butterworth and Chebyshev-I Low Pass Filter Using Approximation, Python, and Proteus, Journal of Signal Processing Systems manuscript, pp.1-16.

Appendix 1

The Theory of the Passive Low-Pass Filter of the Second Order

Let's assume that i_L is the peak value of the total current passing through the inductance, i_C is the peak value of the current passing through the capacitance, i_R is the peak value of the current passing through the resistor.

Also, $Z_L = j\omega L$, $Z_C = \frac{1}{j\omega L}$, $Z = R$ are the corresponding resistances. The voltage gain factor G can be introduced as

$$G(\omega) = \frac{V_{out}(\omega)}{V_{in}(\omega)} \tag{1}$$

where $V_{out} = V_R = V_C, V_{in} = V_L + V_{out}$ $(i_L = \frac{V_L}{Z_L}, i_C = \frac{V_C}{Z_C}, i_R = \frac{V_R}{Z_R})$

Since

$$i_L = i_C + i_R \tag{2}$$

Or $\frac{V_L}{Z_L} = \frac{V_C}{Z_C} + \frac{V_R}{Z_R} = \frac{V_{in} - V_{out}}{Z_L} = V_{out}(\frac{1}{Z_C} + \frac{1}{Z_R})$

The expression for the real part of the gain factor can be reduced to the following:

$$G' \equiv \frac{1}{2} = \frac{1 - x^2}{(1 - x^2)^2 + x^2 Q^2} \tag{3}$$

Where $x = \frac{\omega}{\omega_0}, \omega_0 = \frac{1}{\sqrt{LC}}$, ω_0 is the resonance frequency of the LC circuit, Q is the Quality Factor (opposite to the Damping Ratio) $Q = \frac{1}{R}\sqrt{\frac{L}{C}}$.

For R = 130 Ω, L = 25 mH, and C = 1 μF, ω_0 = 6325 rad/s ~ 1007 Hz, Q ~1.22.

To evaluate the cut-off frequency, we assume that at that frequency the gain factor equals ½ (-3dB):

$$G' \equiv \frac{1}{2} = \frac{1 - x^2}{(1 - x^2)^2 + x^2 Q^2} \tag{4}$$

which results in x ~ 0.709 or ~ 709Hz.

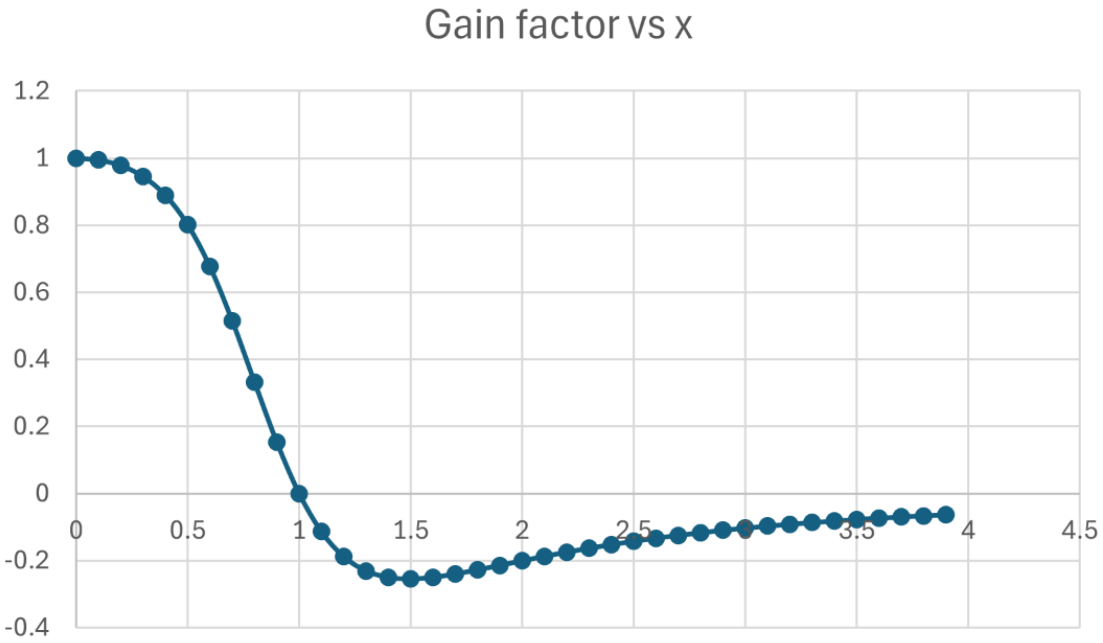

Appendix 2

Python Code Simulating the Square-Wave and its FFT

```
""" Generate a Square Wave
Use scipy.signal.square to create a square wave
Define parameters such as frequency, duration, and sampling rate"""

import numpy as np
import matplotlib.pyplot as plt
from scipy import signal
from scipy.fft import fft, fftfreq, fftshift

# Parameters
frequency = 1000 # Frequency of the square wave in Hz
duration = 0.005 # Duration of the signal in seconds
sampling_rate = 100000 # Sampling rate in Hz
t = np.linspace(0, duration, int(sampling_rate * duration), endpoint=False)

# Create the square wave
square_wave = signal.square(2 * np.pi * frequency * t)

"""      Perform  the  FFT
Use  numpy.fft.fft to compute the FFT of the square wave
Use numpy.fft.fftfreq to get the corresponding frequency values """
# Compute the FFT
fft_result = fft(square_wave)
fft_freq = fftfreq(len(square_wave), 1/sampling_rate)

"""   Shift and Normalize the FFt Output
Use numpy.fft.fftshift to center the zero frequency at the middle of the spectrum
Calculate the magnitude of the FFT result using np.abs()
Normalize the magnitude by dividing by the number of samples """

  # Shift the zero-frequency component to the center of the spectrum

fft_result_shifted = fftshift(fft_result)
fft_freq_shifted = fftshift(fft_freq)

# Calculate the magnitude of the FFT result
magnitude = np.abs(fft_result_shifted) / len(square_wave)

"""       Plot the Results
Plot the original square wave in the time domain
Plot the magnitude of the FFT in the frequency domain """
 # Plotting

```

```
plt.figure(figsize=(12, 6))
plt.subplot(2, 1, 1)
plt.plot(t, square_wave)
plt.title('Square Wave in Time Domain')
plt.xlabel('Time (s)')
plt.ylabel('Amplitude')
plt.subplot(2, 1, 2)
plt.plot(fft_freq_shifted, magnitude)
plt.title('FFT of Square Wave')
plt.xlabel('Frequency (Hz)')
plt.ylabel('Magnitude')
plt.xlim(0,55000)
plt.grid(True)
plt.tight_layout()
plt.show()
```

Appendix 3

Python Code Simulating the Word of LPF

```
import numpy as np
from scipy.signal import butter, lfilter, freqz
import matplotlib.pyplot as plt
def butter_lowpass(cutoff, fs, order=5):
return butter(order, cutoff, fs=fs, btype='low', analog=False)
def butter_lowpass_filter(data, cutoff, fs, order=5):
b, a = butter_lowpass(cutoff, fs, order=order)
y = lfilter(b, a, data)
return y
# Filter requirements.
order = 2
fs = 100000       # sample rate, Hz
cutoff = 1000  # desired cutoff frequency of the filter, Hz
# Get the filter coefficients so we can check their frequency response.
b, a = butter_lowpass(cutoff, fs, order)
# Plot the frequency response.
w, h = freqz(b, a, fs=fs, worN=8000)
#plt.subplot(2, 1, 1)
plt.plot(w, np.abs(h), 'b')
plt.plot(cutoff, 0.5*np.sqrt(2), 'ko')
plt.axvline(cutoff, color='k')
plt.xlim(0, 0.05*fs)
plt.title('Lowpass Filter Frequency Response')
plt.xlabel('Frequency [Hz]')
plt.grid()
# Demonstrate the use of the filter.
# First, make some data to be filtered.
"""T = 5.0         # seconds
n = int(T * fs) # total number of samples
t = np.linspace(0, T, n, endpoint=False)
# "Noisy" data.  We want to recover the 1.2 Hz signal from this.
data = np.sin(1.2*2*np.pi*t) + 1.5*np.cos(9*2*np.pi*t) + 0.5*np.sin(12.0*2*np.pi*t)
# Filter the data, and plot both the original and filtered signals.
y = butter_lowpass_filter(data, cutoff, fs, order)
plt.subplot(2, 1, 2)
plt.plot(t, data, 'b-', label='data')
plt.plot(t, y, 'g-', linewidth=2, label='filtered data')
plt.xlabel('Time [sec]')
plt.grid()
plt.legend()"""
#plt.subplots_adjust(hspace=0.35)
plt.show()
```

Identification of PCL-Degrading Bacteria from the St. Lawrence River

Hannah Calderon, Asher Woodhead[1], David Walsh[2]

[1] Concordia University, Montreal, Canada

[2] Groupe de recherche interuniversitaire en limnologie (GRIL)

Abstract – Microplastic pollution in the St. Lawrence River (SLR) is pervasive yet little is known about the local microbial communities capable of degrading plastics. In this study, we investigated whether bacteria from the SLR can colonize low-density polyethylene (LDPE) or polyethylene terephthalate (PET) and degrade polycaprolactone (PCL). Three bacterial colonies were identified as being able to degrade PCL, two of which were identified as being members of Pseudomonas spp. Our findings suggest local bacteria may contribute to biodegradable plastic degradation and warrant further studies of their enzymes and their potential ability to degrade LDPE.

Introduction

Microplastic pollution in the St. Lawrence River (SLR) is pervasive. A 2020 study at McGill University by Crew et al. found that the St. Lawrence River contains levels of microplastic pollution similar to that of some of the most polluted fresh-water and marine environments in the world [1]. Though not very abundant, various species of algae, fungi, and bacteria have the ability to colonize and degrade various plastics [2-6]. However, little is known about the local microbial communities in the SLR capable of colonizing and degrading plastics.

In this study, we investigated whether bacteria from the SLR can colonize low-density polyethylene (LDPE) or polyethylene terephthalate (PET) and degrade polycaprolactone (PCL). We hypothesized that potential plastic degrading microorganisms (PDMs) would be able to colonize LDPE since it is an abundant plastic type in the SLR [8]. LDPE was also chosen instead of its counterpart HDPE (high density polyethylene) since products composed of LDPE are much thinner than the aforementioned [7, 9]. Additionally, PET was included in the experimental set up since PCL can be used as a method for the identification of possible enzymes capable of degrading PET (since both are hydrolyzable plastics and polyesters) [10, 11]. Therefore, we hypothesized that if there were enzymes degrading PET, they would also be able to degrade PCL.

Experimental Setup

We sampled water and sediment from Verdun Beach (45.4623° N, 73.5603° W) on October 2024, which was then transferred to four 1L containers containing 1 inch of sediment, as well as four PET pieces, four LDPE pieces, and one glass slide (serving as a control), each material strung on separate fishing lines (inspired by a study by Syrandou et al.) [12, 13].

Two containers were incubated in the dark and two in natural light, either with or without the addition of ammonium chloride and sodium phosphate to test the effects of light (light vs dark) and nutrient enrichment (enriched vs. non-enriched) on bacterial colonization. Two containers were filled with deionized filtered water to serve as a control. Carbon was not added in order to increase the chances of the microorganisms using the plastic pieces as a carbon source and because a study by Howard et al found that doing so increased degradation rates [2, 11].

After thirty days, a PET piece, an LDPE piece, and glass piece from each treatment (except the control) were swabbed onto the PCL agar plates to assess PCL degradation potential. The containers were manually

shaken every few days in order to maintain oxygenation [14]. On day 27, a piece of LDPE from the X N.D Treatment was swabbed and varyingly diluted to determine the best dilution series for plating. After thirty days, a PET piece, an LDPE piece and a glass piece were scraped using an inoculation loop, diluted a hundred-fold, and plated on PCL agar plates to test for the presence of PDMs. PCL can be emulsified into an agar solution creating a cloudy agar plate called a PCL agar plate. The presence of a clear zone around a colony indicates PCL degradation [6, 15].

Furthermore, a positive control, provided by Asher Woodhead, consisting of a bacterium which, when plated on a PCL agar plate had already produced a zone of clearing, was also plated as a reference for clear zone identification (Figure 1) [16].

In total, fifteen plates were tested. After six days of incubation in the dark at room temperature, colonies were counted and examined for zones of clearing.

Figure 1. Positive control plated on a PCL agar plate. Asher Woodhead [Photograph] November 29, 2024 [cited 2024 February 17].

Results

Visible Growth and Biofilm Composition

There was no visible growth on any of the substrates on both Nutrient Enriched Treatments (N.L and N.D). Nevertheless, the plastics and the glass did seem slightly more weathered than they were previously. Contrastingly, both treatments without nutrients (X N) seemed to have visible growth on both LDPE and PET, whilst the glass remained seemingly uncolonized. The visible biofilm composition on the LDPE differed from that on the PET; the colonization on the LDPE was uneven, whereas the colonization on the PET was more even (Figures 2 and 3). Additionally, the biofilm on the light treatment (X N.L) was a light brown, whilst it was a darker brown on the dark treatment (X N.D) which likely attests to the presence of algae in the light treatment. The lack of visible colonization of the N. Treatment was likely due to the increase of acidity in the water caused by the addition of the nutrients which could have been mitigated by the addition of a buffer solution [17]. No growth was observed on the controls.

The colonies plated on the PCL agar plates were counted. However, it was difficult due to confluent growth which may have been due to the dilution not being high enough. Nonetheless, it seems that there was some difference in the microbial composition of the biofilms on the glass piece, the PET piece, and the LDPE piece, displayed by the differing colony morphologies as well as by the visible biofilm composition on the N.D Treatment previously mentioned (Figure 4). Further repetition and characterization of the individual colonies would be needed to confirm this, however many studies have shown that the composition of microbial communities varies depending on the type of plastic and that the aforementioned also differ from controls [12, 18].

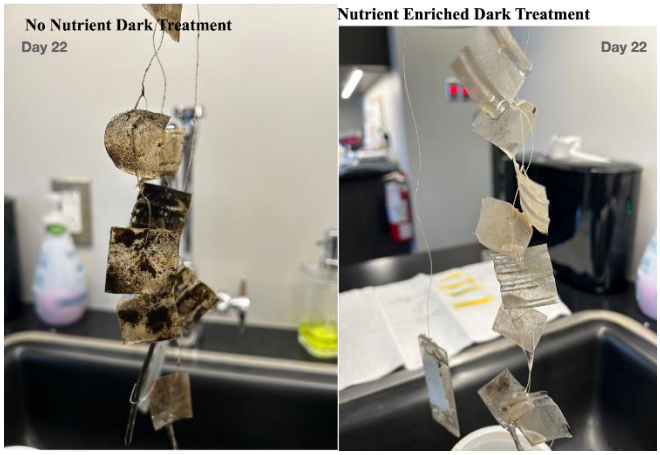

Figure 2. X N.D Treatment (on the left) and N.D Treatment (on the right) photographed on Day 22 of culture.

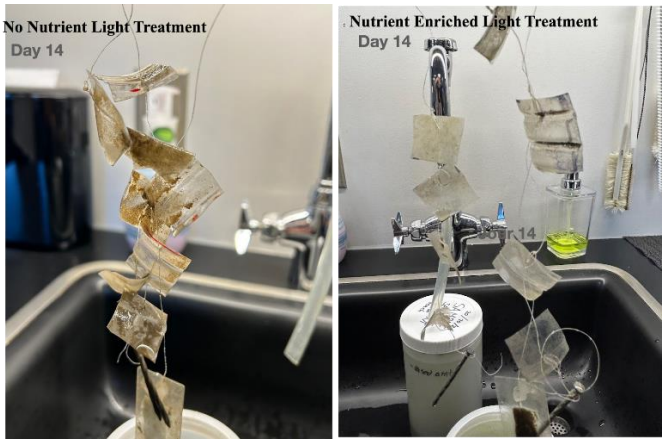

Figure 3. X N. L Treatment (on the left) and N.L Treatment (on the right) photographed on Day 22 of culture.

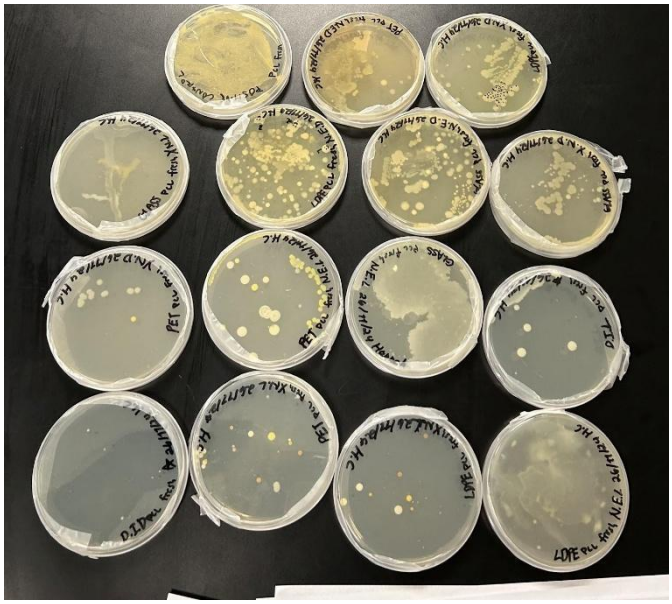

Figure 4. Plated PLC agar plates from all treatments.

PDM Identification

Three clear zones were observed around three colonies sampled from the LDPE plastic cultured in the N.D Treatment (Figure 5). Two colonies were identified through 16s RNA sequencing as belonging to the Pseudomonas genus [19, 20]. Many Pseudomonas species have been found to be able to degrade various plastic types, including LDPE, PET and PCL [2, 21].

Moreover, the first colony was identified, by a full genome sequence, as being *Pseudomonas chlororaphis*, a species that has been identified as being able to degrade LDPE and PCL.

Additionally, various possible plastic degrading enzymes were identified to be present in the aforementioned, including poly(3-hydroxyalkanoate) (PHA) depolymerase, which has been shown to play a role in the degradation of PHA (polyhydroxyalkanoate), a biodegradable plastic [22].

Moreover, enzymes such as lipases, esterases, thioesterases and peroxidases have been proven to play important roles in plastic degradation which were all identified in the genome sequence [23]. Notably, glutathione peroxidase enzymes were identified, which have been found to be a highly efficient LDPE degrader in Rhodococcus spp. in a 2024 study [24].

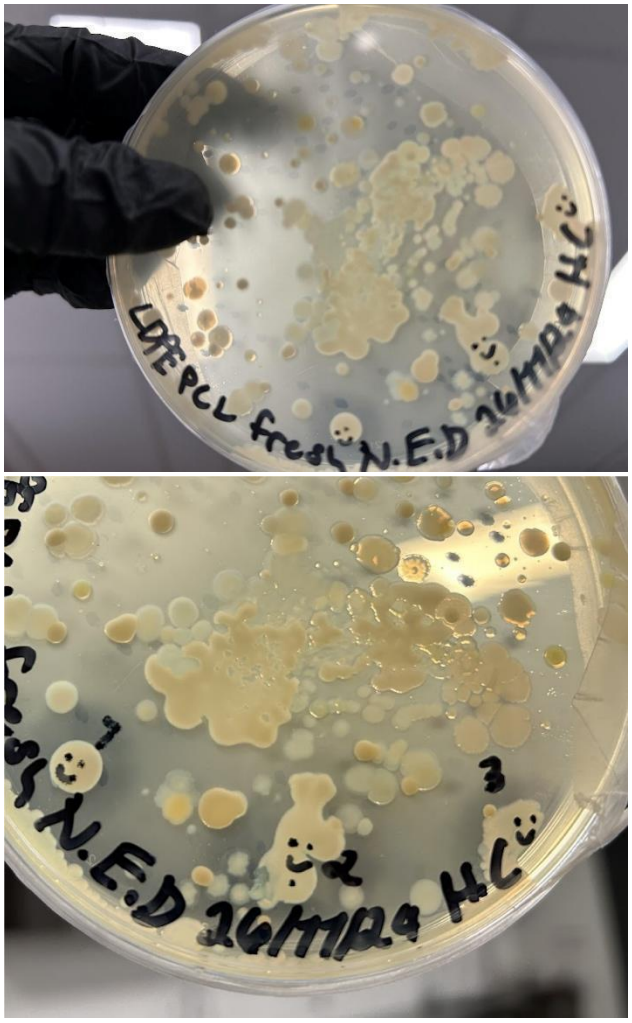

Figure 5. Three colonies possessing surrounding zones of clearing.

Conclusion and Discussion

In conclusion, our findings suggest local bacteria may contribute to biodegradable plastic degradation though sampling various sites across the St. Lawrence River. However, further research is necessary to provide a more complete picture of the microbial communities capable of degrading plastics. Culturing samples in darkness as well as adding nutrients may also improve the likeliness of finding PDMs considering that the only identified PDMs were found on the Nutrient Enriched Dark Treatment. Further research should focus on identifying the possible plastic degrading enzymes present in Pseudomonas chlororaphis and the other Pseudomonas spp. which may expand upon the preexisting list of previously identified plastic degrading enzymes. Additionally, it would be interesting to further explore whether the Pseudomonas spp. identified can degrade LDPE (which may support my hypothesis that the microorganisms in the St Lawrence River are able to colonize and degrade polyethylene due to its abundance in the river) or if their presence on the LDPE plate was unrelated to degradation. Plastic pollution is an important issue and further studies on PDMs is an important step towards finding a method of remediation.

Acknowledgments

A special thank you to Professor Walsh, Asher Woodhead and Dr D'Avignon for all their support.

References

[1] Alex Crew, Irene Gregory-Eaves, Anthony Ricciardi. Distribution, abundance, and diversity of microplastics in the upper St. Lawrence River, Environmental Pollution [Internet] January 2020 [cited 2025 February 17] Volume 260. Available from: https://www.sciencedirect.com/science/article/abs/pii/S0269749119348419

[2] Viel T, Manfra L, Zupo V, Libralato G, Cocca M, Costantini M. [Internet]. Biodegradation of Plastics Induced by Marine Organisms: Future Perspectives for Bioremediation Approaches. Polymers (Basel). [Internet]. June 2023. Volume 15 [cited 2025 February 15] Available from: https://pubmed.ncbi.nlm.nih.gov/37376319/

[3] Sahu S, Kaur A, Khatri M, Singh G, Arya SK. A review on cutinases enzyme in degradation of microplastics. J Environ Manage. [Internet] October 2023. [cited 2024 November 27] Available from: https://pubmed.ncbi.nlm.nih.gov/37797518

[4] Cai, Zeming, Minqian Li, Ziying Zhu, Xiaocui Wang, Yuanyin Huang, Tianmu Li, Han Gong, and Muting Yan. Biological Degradation of Plastics and Microplastics: A Recent Perspective on Associated Mechanisms and Influencing Factors Microorganisms. Microorganisms. [Internet] June 2023. Volume 11 [cited 2025 February 17] Available from: https://doi.org/10.3390/microorganisms11071661

[5] Viljakainen VR, Hug LA. New approaches for the characterization of plastic-associated microbial communities and the discovery of plastic-degrading microorganisms and enzymes. Comput Struct Biotechnol J. [Internet] November 2021 [cited 2024 November 27] Available from: https://pubmed.ncbi.nlm.nih.gov/34900132/

[6] Howard, S.A., McCarthy, R.R. Modulating biofilm can potentiate activity of novel plastic-degrading

enzymes. npj Biofilms Microbiomes [Internet] October 2023. 9(72) [cited 2025 February 17] Available from: https://doi.org/10.1038/s41522-023-00440-1

[7] Arapack FR [Internet] Arapack [cited 2025 February 16] Types de plastiques: comment les différencier? Available from: https://arapack.fr/classification-des-plastiques/

[8] Castañeda Rowshyra A., Avlijas Suncica, Simard M. Anouk, and Ricciardi Anthony. Microplastic pollution in St. Lawrence River sediments. Canadian Daynal of Fisheries and Aquatic Sciences. [Internet] Septembre 2014. 71(12): p.1767-1771. [cited 2024 November 27] Available from: https://cdnsciencepub.com/doi/abs/10.1139/cjfas-2014-0281

[9] Dr Gen D'Avignon. 16 september 2023. Post Doctoral Student. Recommendations as to the location of sampling and the type of plastic to use.

[10] Obrador-Viel T, Zadjelovic V, Nogales B, Bosch R, Christie-Oleza JA. Assessing microbial plastic degradation requires robust methods. Microb Biotechnol. [Internet] April 2024. 17(4) [cited 2024 November 27] Available from: https://pubmed.ncbi.nlm.nih.gov/38568802/

[11] Howard SA, Carr CM, Sbahtu HI, Onwukwe U, López MJ, Dobson ADW, McCarthy RR. Enrichment of native plastic-associated biofilm communities to enhance polyester degrading activity. Environ Microbiol. [Internet] December 2023. 25(12) [cited 2025 February 17] Available from: https://pubmed.ncbi.nlm.nih.gov/37515381/

[12] Silva V, Pérez V, Gillanders BM. [Internet] Short-term plastisphere colonization dynamics across six plastic types. Environ Microbiol. [cited 2024 November 27] December 2023. 25(12), Available from: https://pubmed.ncbi.nlm.nih.gov/37341062/

[13] Syranidou E, Karkanorachaki K, Amorotti F, Repouskou E, Kroll K, Kolvenbach B, Corvini PF, Fava F, Kalogerakis N. Development of tailored indigenous marine consortia for the degradation of naturally weathered polyethylene films. PLoS One. [Internet] August 2017. 12(8). [cited 2025 February 17] Available from: https://pubmed.ncbi.nlm.nih.gov/28841722

[14] Professor David Walsh. July 5 2024. Professor at Concordia. Scientific Supervisor, lending of materials, aid in project planning and experimental set up.

[15] Alberto Contreras-Moll, Theo Obrador-Viel, Rocío Daniela Inés Molina, Maria del Mar Aguiló-Ferretjans, Balbina Nogales, Rafael Bosch, Joseph A. Christie-Oleza, Lack of functional polyester-biodegrading potential in marine versus terrestrial environments evidenced by an innovative airbrushing technique, Journal of Hazardous Materials [Internet] December 2024 . 486. [cited 2025 February 18] Available from: https://www.sciencedirect.com/science/article/pii/S0304389424036458

[16] Asher Woodhead. November 13 2024. Lab work supervisor and aid in project planning.

[17] Jose Pietri & Donald Land. [Internet] Introduction to Buffers. LibreTexts. [cited 2024 November 27] Available from: https://chem.libretexts.org/Bookshelves/Physical_and_Theoretical_Chemistry_Textbook

[18] Josefine Hansen, Jette Melchiorsen, Nicole Ciacotich, Lone Gram, Eva C Sonnenschein, Effect of polymer type on the colonization of plastic pellets by marine bacteria, FEMS Microbiology Letters [Internet] March 2021. 368(5) [cited 2025 February 17] Available from: https://doi.org/10.1093/femsle/fnab026

[19] Zymo Research. Quick-DNA™ Miniprep Plus Kit DNA Purification Purify high quality total DNA from a variety of sample types.

[20] National Library of Medicine. Web Blast [Internet]. Bethesda MD; NCBI [cited 2025 February 17] Available from: https://blast.ncbi.nlm.nih.gov/Blast.cgi

[21] Kučić Grgić, Dajana, Martina Miloloža, Vesna Ocelić Bulatović, Šime Ukić, Miroslav Slouf, and Veronika Gajdosova. Screening the Efficacy of a Microbial Consortium of Bacteria and Fungi Isolated from Different Environmental Samples for the Degradation of LDPE/TPS Films. Separations [Internet] January 2023. 10(2). [cited 2025 February 17] Available from: https://www.mdpi.com/2297-8739/10/2/79

[22] Mohanan N, Wong MC, Budisa N, Levin DB. Polymer-Degrading Enzymes of Pseudomonas chloroaphis PA23 Display Broad Substrate

Preferences. Int J Mol Sci. [Internet] February 2023. 24(5). [cited 2025 February 18] Available from: https://pmc.ncbi.nlm.nih.gov/articles/PMC10003648/

[23] Imran Khan, Jayati Ray Dutta, Ramakrishnan Ganesan, Lactobacillus sps. lipase mediated poly (ε-caprolactone) degradation, International Journal of Biological Macromolecules. [Internet] February 2017. 95. [cited 2025 February 18] Available from: https://doi.org/10.1016/j.ijbiomac.2016.11.040.

[24] Zhen Rong, Zhi-Hao Ding, Yue-Hong Wu, Xue-Wei Xu, Degradation of low-density polyethylene by the bacterium Rhodococcus sp. C-2 isolated from seawater, Science of The Total Environment. [Internet] October 2023. 907. [cited 2025 February 18] Available from: https://doi.org/10.1016/j.scitotenv.2023.167993

Impact of Climate Change and Socioeconomic Factors on Dengue Incidence in Southern Asia, Southeast Asia, and South America

Thomas Deleuze-Bisson, Antoine Larocque, Trong Don Nguyen, Mohamed Younes

Abstract – Dengue fever is one of the most significant arboviral diseases impacting modern society. It poses a serious threat in tropical regions, where mosquitoes—primarily *Aedes aegypti*—thrive as the vectors of transmission. Annually, 400 million infections occur, with 100 million people falling ill. In this study, we investigated how temperature, vapour pressure, soil moisture, and precipitation influenced dengue incidence in various tropical and subtropical countries (Thailand, Vietnam, Sri Lanka, Singapore, the Philippines, Panama, Nicaragua, Laos, Jamaica, El Salvador, Ecuador, Costa Rica, Cambodia, and Belize) from 2010 to 2022. Moreover, we assessed how climate change may affect dengue incidence in the future. We applied multiple linear regressions to investigate the relationship between climate variables and dengue cases. The tropical and subtropical countries studied showed significant relationships ($p < 0.05$) and a positive correlation between vapour pressure, minimum monthly temperature, monthly precipitation, soil moisture, and the number of dengue cases per 1,000 people. Leveraging this data, we constructed a model, meeting all required statistical assumptions, that predicted a significant increase of 18.6% in infection cases due to climate change in a hypothetical year in which global temperatures rose by 2°C. Finally, an additional multiple regression analysis incorporating previously examined weather variables, electricity use, urban population percentage, and the Human Development Index (HDI) revealed that urban population was significantly positively correlated with infections per 1,000 individuals, while electricity consumption per capita as well as HDI were not significantly correlated with infection rates.

Introduction

Dengue fever is a prominent disease in tropical regions, sparking various outbreaks (WHO, 2024). Some of its symptoms include severe headache, nausea, fatigue, and fever (Government of Canada, 2014). Treating this virus is problematic due to the lack of a reliable vaccine, with both CYD-TDV (Dengvaxia®) and Qdenga being ineffective in terms of long-term protection against dengue fever (Lee et al., 2024). This issue is more pronounced in countries that have difficulties in limiting the spread of this disease or treating people who fall ill due to limited resources, particularly South American and South Asian nations (Zhang et al., 2025).

The incidence of this disease is mainly reported due to infection from the bite of Aedes aegypti mosquitoes (Brady et al., 2012). Warmer temperatures can lead to shorter periods for the virus to mature in the mosquito, increasing the spread of dengue (Liu-Helmersson et al., 2014).

Moreover, increases in temperature directly accelerate mosquito development time and, therefore, the rate of dengue virus spread in human populations.

Dengue transmission vectors reproduce in small ponds, as they prefer humid areas to breed. Thus, precipitation is also a major variable since it creates ideal breeding grounds for *Aedes aegypti* mosquitoes, particularly when rainwater pools in containers and becomes stagnant (Ebi & Nealon, 2016). As a result, rainfall patterns, especially in tropical areas, are strongly linked to dengue outbreaks (Brady et al., 2012). Past studies have shown that there is an existing correlation between rainfall and infection cases, as regions experiencing

frequent or heavy seasonal rainfall tend to have more dengue cases (Chaves, 2012).

Since climate change alters precipitation and temperature patterns in tropical regions, it may contribute to global changes in dengue fever infections (Ryan et al., 2019). Moreover, regions that have never experienced any incidence of this disease could become at risk in the next few years due to the mosquito vector's spread in regions previously inhospitable to their growth (Ebi & Nealon, 2016). The impact of climate change on dengue incidence remains uncertain in tropical countries due to various complex relationships between the disease, climate conditions, and socioeconomic factors (Colón-González et al., 2013; Marengo et al., 2023).

While previous studies have managed to establish numerous links between various weather variables and dengue fever cases, there remains a lack of understanding of the effects of changes in environmental factors on the spread of the disease, especially in tropical regions (Liu-Helmersson et al., 2014; Ryan et al., 2019). An analysis that incorporates socioeconomic factors and multiple climate variables may refine climate change predictions of dengue incidence and pioneer innovative solutions to limit the spread of the disease. Given the need to push further research on dengue fever, we will aim to identify the relationship between dengue and many climate variables (temperature, vapour pressure, precipitation, and soil moisture) as well as with socio-demographic variables (electricity consumption per capita, urban population percentage, agricultural land percentage). We will also forecast dengue case trends over the coming years based on the predicted changes in these variables.

Methods

All raw data was collected from open-source databases. Countries' populations and socioeconomic factors (percent urban population, electricity power per capita (kWh), and percent agricultural land) were retrieved from the World Bank (World Bank Group, 2025), and the Human Development Index from the United Nations (UNDP, 2024). These socioeconomic factors were chosen to capture a wide range of socioeconomic realities (disparity, income, demographic proxies, access to electricity, etc.). Data related to dengue infections was retrieved from OpenDengue (Clarke et al., 2023), and monthly climate variables (vapour pressure, soil moisture, precipitation, and minimum monthly temperature) from TerraClimate (Abatzoglou et al., 2018). Monthly data for these variables from 2010 to 2022 were gathered for 15 tropical countries (Thailand, Vietnam, Sri Lanka, Singapore, the Philippines, Panama, Paraguay, Nicaragua, Laos, Jamaica, El Salvador, Ecuador, Costa Rica, Cambodia, and Belize). These countries were chosen for their moderate territorial size, lessening the overall variation in weather. This is because, in larger countries, different regions experience varying weather conditions, which may interfere with the analysis.

Data were first visualized with scatterplots and time series in R version 4.5.0 with the ggplot2 package. Outliers were removed, especially those with zero and exceedingly high values, as they caused skewed results and flawed statistical inference during the analysis and were unlikely to result from climate variability (Shihada et al., 2017). Dengue cases were also standardized by calculating dengue incidence per 1,000 people, ensuring that the data were scaled to the population of each country.

Statistical tests were then applied to identify patterns and correlations in R, while maps were made with Python version 3.21, using the Geopandas module. A multiple linear regression was performed with climate variables (vapour pressure, minimum temperature, precipitation, and soil moisture), month, and dengue incidence category as predictors of log-transformed dengue cases per 1,000 people. To meet the homoscedasticity of residuals, we categorized countries into "low" and "high" dengue incidence categories, where "high" dengue incidence was defined as an average log-transformed number of dengue cases per 1,000 people greater or equal to -5.

The linear relationship between predictors and the log of dengue cases per 1,000 people was assessed with scatterplots showing the relationship between the log of dengue cases per 1,000 people and each predictor. Dengue cases per 1,000 people were log-transformed to ensure normality of residuals, which was assessed with a histogram and a Q-Q plot. The homoscedasticity of residuals was assessed with scatterplots showing the relationship between residuals and each predictor. The spatial independence of residuals was assessed with Moran's I spatial autocorrelation test for each month between 2010 and 2022, while the temporal independence of residuals was assessed with a time series of the residuals. Multicollinearity was assessed with the VIF function from the car package in R.

Then, climate change predictions were made with the following multilinear regression model:

$$\log(cases) = \beta 1 \cdot \text{Country } 1 + \cdots + \beta 15 \cdot \text{Country } 15 + \beta 15 \cdot \text{vap} + \beta 16 + 1 \cdot \text{tmin} + \beta 17 + 2 \cdot \text{ppt} + \beta 18 + \beta 18 \text{ soil} + \beta 20 \text{ month} + \beta 21 \text{ month } 2 + \varepsilon \quad (1)$$

Cases represent the number of cases per 1,000 people, vap is vapour pressure (kPa), tmin is minimum temperature (°C), ppt is precipitation (mm), and soil is soil moisture (mm).

To make predictions, climate variables in a +2°C global warming scenario from the TerraClimate dataset were used. Then, the average 2010-2022 dengue cases were compared to the predicted dengue cases in a +2°C global warming scenario.

To determine whether socioeconomic factors have an influence on dengue incidence directly or by interacting with climate variables, an analysis was made based on a multilinear regression that used interaction terms between socioeconomic and climate factors for each socioeconomic factor. To minimize multicollinearity, climate and socioeconomic variables were standardized by centering them, which can be done by subtracting each variable from the mean. All statistical assumptions (linear relationship between predictors and the log of cases per 1,000 people, normality of residuals, homoscedasticity of residuals, and independence of residuals) were verified in a similar manner as the previous linear regressions.

Results

Four scatterplots were generated by plotting vapour pressure, soil moisture, precipitation, and minimum temperature (x-axis) against log-transformed dengue incidence (y-axis). All variables exhibited positive correlations with the dependent variable ($p_{vap} < 2e\text{-}16$, $p_{tmin} < 2e\text{-}16$, $p_{soil} = 5.65e\text{-}7$, $p_{ppt} = 9.43e\text{-}14$).

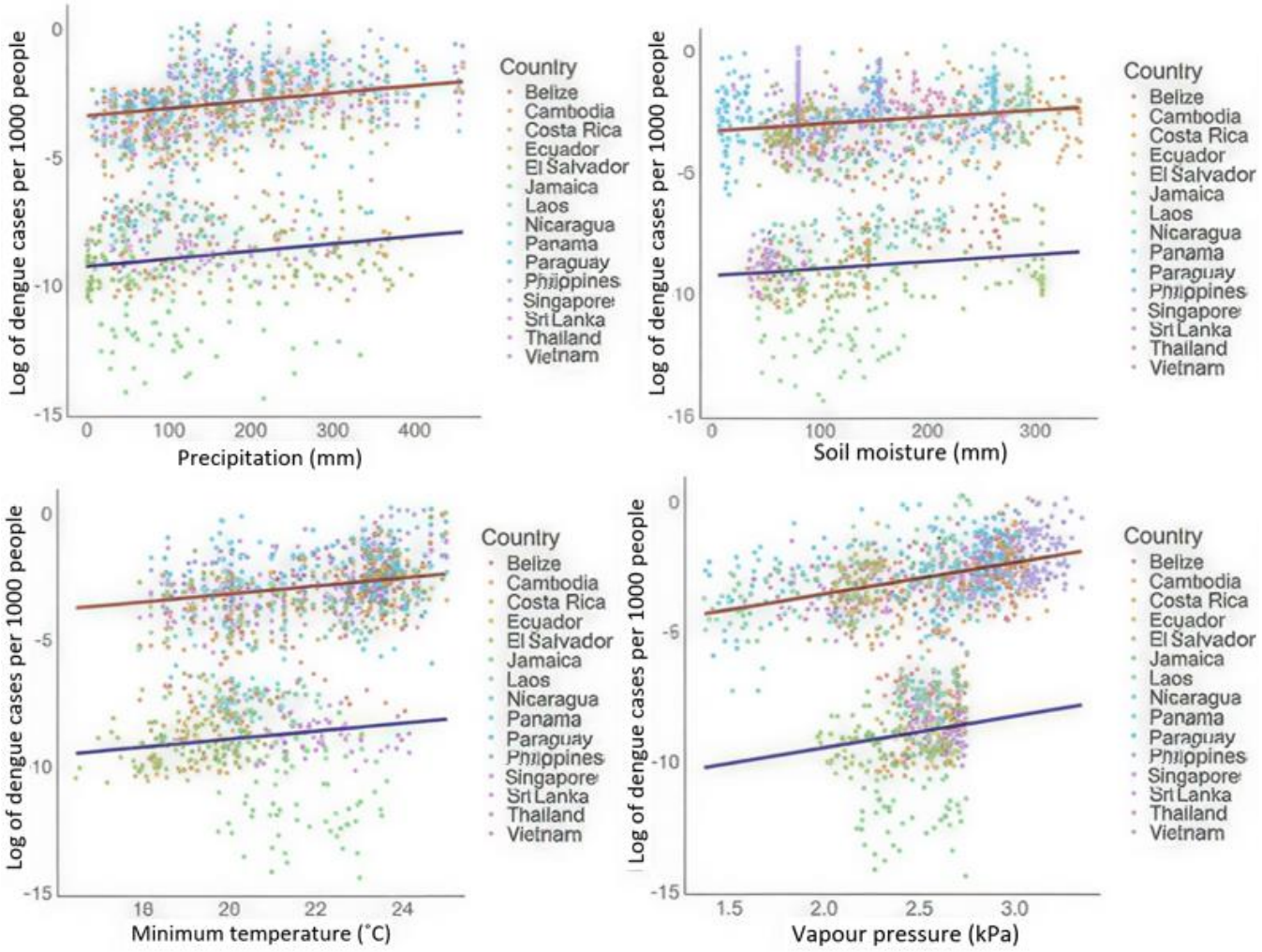

Figure 1. Relationship between climate variables and log of dengue cases per 1000 people.

The multilinear regression revealed a significant positive correlation between dengue cases per 1,000 individuals and precipitation ($\beta = 0.0030$, $p < 2e\text{-}16$). It also revealed a significant positive correlation between dengue cases per 1,000 individuals and soil moisture ($\beta = 0.0029$, $p = 3.61e\text{-}11$), dengue cases per 1,000 people and minimum temperature ($\beta = 0.1579$, $p = 1.72e\text{-}15$), and dengue cases per 1,000 people and ambient vapour pressure ($\beta = 1.219$, $p < 2e\text{-}16$). The R^2 value was 0.8485 for the overall analysis.

Using equation 1, it was found that the hypothetical year presenting an increase of 2°C in global temperature would result in a total increase of 18.6% in dengue cases in the studied countries. However, not all countries show an increase in dengue cases (Appendix C).

Due to climate change (+2°C scenario), on average, minimum temperature increases by 0.825°C, vapour pressure increases by 0.233 kPa, while precipitation and soil moisture decrease by 19.9 mm and 4.7 mm, respectively.

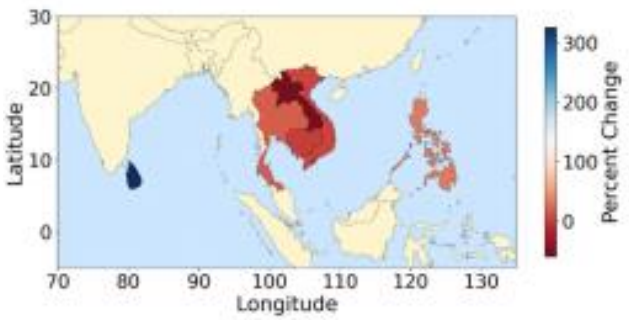

Figure 2. Climate change prediction of dengue incidence in South-East Asia.

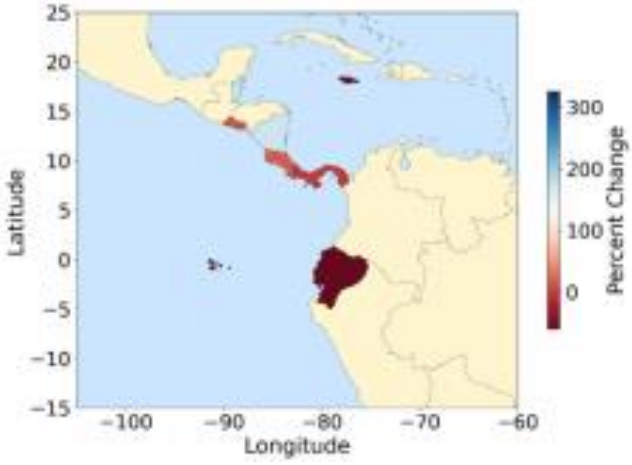

Figure 3. Climate change predictions of dengue incidence in Central America.

The Human Development Index and the electricity power per capita were not significantly correlated with the log of dengue cases. None of the interaction terms between the Human Development Index and climate variables was significant. The same was true for the interaction terms between the electricity power per capita and climate variables.

The percentage of urban population was significantly positively correlated with the log of dengue cases. Moreover, the interaction term between the percentage of urban population and vapour pressure was significant and negative. The other interaction terms with climate variables were not statistically significant.

Discussion

Our multilinear regression analysis with climate variables shows statistically significant and positive relationships between all climate variables and dengue cases. Notably, vapour pressure reflects absolute humidity, meaning that higher vapour pressure indicates more moisture in the air. Hence, higher vapour pressure slows down evaporation, causing water to stay longer in containers, which creates ideal breeding grounds for mosquitoes. This supports findings in current literature on *Aedes aegypti* life cycles and breeding habits (Ferede et al., 2018).

We also found a strong positive correlation between precipitation and dengue cases. This result is also consistent with existing literature, as rainwater accumulation tends to cause water stagnation, which serves as an ideal breeding ground for mosquitoes. Consequently, areas with high rainfall tend to exhibit greater mosquito population densities.

Similarly, the positive relationship between soil moisture and dengue incidence may be explained by the mosquito's life cycle. Higher soil moisture could indicate good breeding conditions for mosquitoes, leading to more dengue cases.

Additionally, our data revealed a strong positive correlation between minimum temperature and dengue incidence. This can be explained by the fact that *Aedes aegypti* mosquitoes thrive in temperatures between 25 °C and 30 °C, while temperatures above 40 °C can kill adult mosquitoes and inhibit larval development (Reiskind and Zarrabi, 2012). In many tropical countries, minimum temperatures during the hotter months often fall just below this optimal range. As these minimum temperatures rise into the 25 to 30 °C range, the period during which mosquitoes can thrive at

peak capacity is extended. An additional explanation is that warmer temperatures speed up the *Aedes aegypti* mosquito's life cycle—eggs hatch faster, larvae mature quicker, and adult mosquitoes become more active—leading to an increase in bites and faster transmission of dengue fever. Furthermore, higher temperatures can decrease the extrinsic incubation time, which is the time required for a mosquito to become infectious after blood ingestion of an infected host (Kamiya et al., 2020).

As for our multilinear analysis, we found that a +2°C climate change scenario would lead to an 18.6% surge in dengue incidence. This suggests that rising temperatures alongside their repercussions on the environment are associated with increased dengue transmission in South America and Southeast Asia. This supports our hypothesis that climate change contributes to the spread of the disease. Moreover, these findings align with existing literature, highlighting the impact of elevated temperatures on dengue spread, and emphasizing the negative effects of climate change on vulnerable communities worldwide (Feng et al., 2024).

However, it is important to mention that these results were not uniform across all countries. In fact, some countries actually showed a decrease in dengue cases. This can be explained by the fact that climate change is generally associated with lower precipitation and soil moisture. Hence, in some countries (Panama, Ecuador, Jamaica, and Laos), those factors outweighed the increase in temperature and led the model to predict a decrease in dengue cases. The rest of the countries exhibited results consistent with our hypothesis and showed an increase in dengue cases due to the rise in temperature, directly affecting minimum temperature, leading to the 18.6% predicted increase in dengue cases. This finding suggests that the increase in dengue cases over the next few years cannot be generalized on a global scale and must be studied regionally, as some regions or countries might experience a different outcome from the predicted one, as the model proved.

Our results also indicate that countries where a higher percentage of the population lives in urban settings tend to face an increased number of dengue outbreaks. This suggests that the majority of dengue patients contract the virus in cities which may hold a greater mosquito population because of increased human presence. This stresses the importance of using effective tools and strategies in densely populated areas to limit the spread of the disease. In fact, many countries have already started to do so. Some of the innovative strategies they use include mosquito nets, awareness campaigns across cities, larvicides, and ULV fogging during outbreak periods. Some countries have also tried to introduce Wolbachia-infected individuals in mosquito-infested countries to decimate the infected population (WHO, 2025). Past studies have shown that the introduction of Wolbachia-infected mosquitoes in the global population of the species led to a reduction of 86.2% in dengue-related hospitalizations in Indonesia (Utami et al., 2021).

The socioeconomic multilinear regression results stress the relevance of incorporating such data when making climate change predictions of dengue cases. Indeed, socioeconomic factors can be correlated with dengue incidence directly, but they can also interact with climate variables to shape the relationship between climate variables and dengue incidence. It is also important to consider socioeconomic factors when assessing the vulnerability of countries to dengue. Indeed, not all countries have the same resources to limit dengue propagation and treat infected patients. The Global Health Index is a useful starting point to determine how different countries have the capacity to deal with dengue cases (Razavi et al., 2020).

Despite the statistical significance of our findings, certain limitations should be acknowledged. First, data points where dengue cases were reported as zero have been omitted, as they were assumed to be errors or outliers, which may have introduced bias. Another limitation of our study is that the data were aggregated at the country level rather than at a finer spatial resolution, which may have skewed the results for larger countries with diverse climates, as regional and local differences are not reflected in the national averages.

For future research, it would be interesting to analyze data at smaller scales, such as the regional level, as that would provide a better representation of how climate fluctuations impact dengue incidence in specific areas. Studying the differences in dengue vulnerability between urban and rural populations, along with other socioeconomic factors, could help identify new variables that significantly impact communities. It would also be relevant to assess impacts of dengue on rather vulnerable communities, such as those living in informal settlements, to assess in what ways is the transmission of the virus different in such a socioeconomic context.

Conclusion

In conclusion, the purpose of this research was to understand the impact of climate change and socioeconomic factors on dengue cases. Our findings showed strong positive correlations between several climate factors and dengue cases, particularly highlighting the relationships between vapour pressure, soil moisture, temperature, and precipitation and dengue incidence in various countries in Southeast Asia and South America. This study highlights the urgent need for action in these regions, as a 2°C increase in global temperatures is predicted to lead to an 18.6% rise in dengue incidence across the countries studied. This underscores the significant impact of climate change on public health, particularly in tropical regions where dengue fever is most prevalent. Moreover, dengue incidence was positively correlated with urbanization and socioeconomic factors that can interact with climate variables to shape their relationship with dengue incidence. Moving forward, climate-focused strategies that integrate socioeconomic considerations will be critical in reducing national vulnerability to dengue outbreaks. Equally important will be increased public awareness, sustained investment in research, and the development of effective technologies to support long-term prevention and response efforts.

References

[1] Abatzoglou, John T., et al. "TerraClimate, a High-Resolution Global Dataset of Monthly Climate and Climatic Water Balance from 1958–2015." Scientific Data. Accessed June 26, 2025. https://doi.org/10.1038/sdata.2017.191

[2] Brady, Oliver J., et al. "Refining the Global Spatial Limits of Dengue Virus Transmission by Evidence-Based Consensus." PLOS Neglected Tropical Diseases. Accessed June 26, 2025. https://doi.org/10.1371/journal.pntd.0001760

[3] Chaves, Luis F., et al. "Social Exclusion Modifies Climate and Deforestation Impacts on a Vector-Borne Disease." PLOS Neglected Tropical Diseases. Accessed June 26, 2025. https://doi.org/10.1371/journal.pntd.0000176

[4] Clarke, John, et al. "OpenDengue: Data from the OpenDengue Database." Figshare. Accessed June 26, 2025. https://doi.org/10.6084/m9.figshare.24259573

[5] Colón-González, Felipe J., et al. "The Effects of Weather and Climate Change on Dengue." PLOS Neglected Tropical Diseases. Accessed June 26, 2025. https://doi.org/10.1371/journal.pntd.0002503

[6] Ebi, Kristie L., and James Nealon. "Dengue in a Changing Climate." Environmental Research. Accessed June 26, 2025. https://doi.org/10.1016/j.envres.2016.07.026.

[7] Feng, Fan, et al. "Temperature-Driven Dengue Transmission in a Changing Climate: Patterns, Trends, and Future Projections." GeoHealth. Accessed June 26, 2025. https://doi.org/10.1029/2024gh001059.

[8] Ferede, Getachew, et al. "Distribution and Larval Breeding Habitats of Aedes Mosquito Species in Residential Areas of Northwest Ethiopia." Epidemiology and Health. Accessed June 26, 2025. https://doi.org/10.4178/epih.e2018015.

[9] Government of Canada. Dengue Fever. Accessed June 26, 2025. https://www.canada.ca/en/public-health/services/infectious-diseases/viral-haemorrhagic-fevers/ d engue-fever/symptoms.html.

[10] Heinisch, Michele R. S., et al. "Seasonal and Spatial Distribution of Aedes aegypti and Aedes albopictus in a Municipal Urban Park in São Paulo, SP, Brazil." Acta Tropica. Accessed June 26, 2025. https://doi.org/10.1016/j.actatropica.2018.09.011.

[11] Hii, Yien Ling, et al. "Forecast of Dengue Incidence Using Temperature and Rainfall." PLOS Neglected Tropical Diseases. Accessed June 26, 2025. https://doi.org/10.1371/journal.pntd.0001908.

[12] Intergovernmental Panel on Climate Change (IPCC). Climate Change 2023 Synthesis Report. Accessed June 26, 2025. https://www.ipcc.ch/report/ar6/syr/downloads/report/IPCC_AR6_SYR_LongerReport.pdf.

[13] Lee, Meng F., et al. "Current Status of the Development of Dengue Vaccines." Vaccine: X. Accessed June 26, 2025.https://doi.org/10.1016/j.jvacx.2024.100604.

[14] Linares, Elaine M., et al. "Immunospot Assay Based on Fluorescent Nanoparticles for Dengue Fever Detection." Biosensors & Bioelectronics. Accessed June 26, 2025. https://doi.org/10.1016/j.bios.2012.08.005.

[15] Liu-Helmersson, Jing, et al. "Vectorial Capacity of Aedes aegypti: Effects of Temperature and Implications for Global Dengue Epidemic Potential." PLOS ONE. Accessed June 26, 2025. https://doi.org/10.1371/ journal.pone.0089783.

[16] Kamiya, Takuya, et al. "Temperature-Dependent Variation in the Extrinsic Incubation Period Elevates the Risk of Vector-Borne Disease Emergence." Epidemics. Accessed June 26, 2025. https://doi.org/10.1016/j.epidem.2019.100382.

[17] Marengo, José A., et al. "Changes in Climate and Land Use Over the Amazon Region: Current and Future Variability and Trends." Frontiers in Earth Science. Accessed June 26, 2025. https://doi.org/10.3389/feart.2018.00228.

[18] Mercier, Aurélie, et al. "Impact of Temperature on Dengue and Chikungunya Transmission by the Mosquito Aedes albopictus." Scientific Reports. Accessed June 26, 2025. https://doi.org/10.1038/s41598-022-10977-4.

[19] NOAA. National Centers for Environmental Information (NCEI). Accessed June 26, 2025. https://www.ncei.noaa.gov/.

[20] Utami, A. P., et al. "Efficacy of Wolbachia-Infected Mosquito Deployments for the Control of Dengue." The New England Journal of Medicine. Accessed June 26, 2025. https://doi.org/10.1056/NEJMoa2030243.

[21] United Nations Development Programme (UNDP). Human Development Report 2023/24: Breaking the Gridlock—Reimagining Cooperation in a Polarized World. Accessed June 26, 2025. https://hdr.undp.org/content/human-development-report-2023-24.

[22] Ryan, Sadie J., et al. "Global Expansion and Redistribution of Aedes-Borne Virus Transmission Risk with Climate Change." PLOS Neglected Tropical Diseases. Accessed June 26, 2025. https://doi.org/10.1371/journal.pntd.0007213.

[23] Sentian, Juliana, et al. "Climate Change Scenarios over Southeast Asia." APN Science Bulletin. Accessed June 26, 2025. https://doi.org/10.30852/sb.2022.1927.

[24] Stebbins, R. Carter, et al. "The Effectiveness of Community Bed Net Use on Malaria Parasitemia among Children Less Than 5 Years Old in Liberia." The American Journal of Tropical Medicine and Hygiene. Accessed June 26, 2025. https://doi.org/10.4269/ajtmh.17-0619.

[25] World Health Organization (WHO). Improving Data for Dengue. Accessed June 26, 2025. https://www.who.int/activities/improving-data-for-dengue.

[26] World Health Organization (WHO). Dengue - Global Situation. Accessed June 26, 2025. https://www.who.int/emergencies/disease-outbreak-news/item/2024-DON518.

[27] World Bank. World Bank Group. Accessed June 26, 2025. https://www.worldbank.org/.

[28] Zhang, Wei-Xiang, et al. "Assessing the Global Dengue Burden: Incidence, Mortality, and Disability Trends over Three Decades." PLOS Neglected Tropical Diseases. Accessed June 26, 2025. https://doi.org/10.1371/journal.pntd.0012932.

Vector Formulation of Refraction for Simulation

Aryan Shadzi

Abstract – The paper presents a vectorial formulation of refractive phenomena for ray tracing. Traditional methods tend to rely on angular quantities which can have significant computational overhead caused by the cost of evaluating trigonometric functions. The model's reformulation of Snell's law in vectorial form provides a more optimized approach to refraction in ray tracing, enabling efficient computation of the refracted ray direction. Additionally, the model implements pseudo-random ray transmission following the Fresnel's equation and a simple Cauchy approximation of IOR chromatic dispersion. The model, implemented in C++ with OpenGL, demonstrated visually accurate reflection and refraction when compared with a similar setup in Blender, a well-known rendering platform. The chromatic dispersion model remains purely mathematical and has yet to be tested.

Introduction

Light modeling became increasingly important during the twentieth century and is now central in scientific simulation and computer graphics. It is used to simulate phenomena that are difficult to reproduce experimentally, to preview realistic architectural images before construction, and to improve visual quality in films and video games. One challenging phenomenon to simulate is refraction [1]. Snell's law is traditionally expressed using incidence angles, but modern simulation pipelines operate on vectors. Using Snell's law in its angle form can require inverse trigonometric functions, which are computationally expensive. In this paper, Snell's law and the Fresnel equations are rewritten in a vector framework suitable for simulation. The objective is to derive a model capable of reproducing refraction, reflection, total internal reflection, and chromatic dispersion.

Context and Variables

Consider a light ray crossing the boundary between two media with incidence angle θ_1 measured with respect to the surface normal $\hat{n}$. Depending on the refractive indices n_1 and n_2 of the two media, the ray is reflected or refracted at an angle θ_2. The refractive index of a medium is defined as the ratio between the speed of light in vacuum and the speed of light in the medium, i.e., $n = \frac{c}{v}$ [2].

In a vector-based simulation, angles θ_1 and θ_2 are replaced by the unit direction vectors of the incident and transmitted rays, denoted $\hat{v}_1$ and $\hat{v}_2$, to avoid explicit angular computations.

To simulate chromatic effects, each ray is associated with a wavelength λ expressed in micrometers. For simplicity, λ is assumed constant across media boundaries. The refractive index is modeled as a function $n(\lambda, n_{avg})$ relating wavelength to the average refractive index of the material. In physical optics, the frequency of light remains constant across media boundaries, while the wavelength changes according to the change in propagation speed. However, in this model, light is treated under a monochromatic ray approximation in which wavelength-dependent dispersion effects are not explicitly propagated across interfaces, allowing light to be modeled as geometric rays for computational efficiency [1]. The refractive index is treated as a wavelength-dependent property, n=n(wavelength), and is modeled using empirical dispersion relations such as the Cauchy or Sellmeier equations [3].

Derivation of the Refracted Direction Vector

Snell's law states that

$$n_1 sin(\theta_1) = n_2 sin(\theta_2).$$

To express this relation in vector form, an equivalent expression for $sin(\theta)$ is required. Let $\hat{k}$ be a unit vector perpendicular to the surface normal $\hat{n}$ and lying in the plane defined by $\hat{n}$ and the incident ray direction. Then

$$sin(\theta) = \hat{v} \cdot \hat{k} \quad (1)$$

substituting into Snell's law yields

$$n_1(\hat{v}_1 \cdot \hat{k}) = n_2(\hat{v}_2 \cdot \hat{k}).$$

Define

$$M = \frac{n_1}{n_2}\left(\hat{v}_1 \cdot \hat{k}\right) = \hat{v}_2 \cdot \hat{k}. \tag{2}$$

Since $\hat{v}_2$ is a unit vector and $\hat{k} \perp \hat{n}$,

$$\left(\hat{v}_2 \cdot (-\hat{n})\right)^2 + \left(\hat{v}_2 \cdot \hat{k}\right)^2 = 1.$$

Thus,

$$\hat{v}_2 \cdot (-\hat{n}) = \sqrt{1 - M^2}. \tag{3}$$

The refracted direction vector is therefore

$$\hat{v}_2 = M\hat{k} - \hat{n}\sqrt{1 - M^2}. \tag{4}$$

If $|M| > 1$, then $1 - M^2 < 0$ and the square root is not real. Physically, this indicates that refraction does not occur and the ray undergoes total internal reflection (TIR) [4].

In three dimensions, there are infinitely many vectors perpendicular to $\hat{n}$, so $\hat{k}$ must be constrained to lie in the plane of incidence (the plane spanned by $\hat{n}$ and $\hat{v}_1$). Let the normal to that plane be

$$\hat{N} = \hat{n} \times \hat{v}_1.$$

Then $\vec{k}$ can be defined by

$$\hat{k} = (\hat{n} \times \hat{v}_1) \times \hat{n}. \tag{5}$$

All direction vectors are assumed normalized.

Derivation of the Reflected Direction Vector

For reflection, the law of specular reflection states that the angle of incidence equals the angle of reflection with respect to the normal [5]. Using vector geometry, the reflected direction is

$$\hat{v}_2 = \hat{v}_1 - 2(\hat{v}_1 \cdot \hat{n})\hat{n}. \tag{6}$$

This expression is used directly in the case of total internal reflection.

Fresnel Equations

Reflection and refraction are not binary: even without TIR, part of the incident light is reflected while the remainder is transmitted. For unpolarized light reflectance is calculated by:

$$R = \frac{R_s + R_p}{2}.$$

The Fresnel reflectances for s- and p-polarization are

$$R_s = \left|\frac{n_1 cos\theta_1 - n_2 cos\theta_2}{n_1 cos\theta_1 + n_2 cos\theta_2}\right|^2,$$
$$R_p = \left|\frac{n_1 cos\theta_2 - n_2 cos\theta_1}{n_1 cos\theta_2 + n_2 cos\theta_1}\right|^2.$$

where Rs and Rp are the Fresnel reflection coefficient for s-polarization and the Fresnel reflection light coefficient for p-polarized respectively [1].

In vector form, the cosine is the component along the normal:

$$cos\theta_1 = -\hat{v}_1 \cdot \hat{n}, \qquad cos\theta_2 = \sqrt{1 - M^2}.$$

Thus,

$$R_s = \left|\frac{-n_1(\hat{v}_1 \cdot \hat{n}) - n_2\sqrt{1 - M^2}}{-n_1(\hat{v}_1 \cdot \hat{n}) + n_2\sqrt{1 - M^2}}\right|^2, \tag{7}$$

$$R_p = \left|\frac{n_1\sqrt{1 - M^2} - n_2(-\hat{v}_1 \cdot \hat{n})}{n_1\sqrt{1 - M^2} + n_2(-\hat{v}_1 \cdot \hat{n})}\right|^2. \tag{8}$$

The transmitted intensity is

$$T = 1 - R. \tag{9}$$

Chromatic Dispersion

Chromatic dispersion arises from the wavelength dependence of the refractive index. Most tabulated refractive indices are measured at a wavelength of $\lambda_0 = 0.589\,\mu m$. The dispersion function is modeled using the relationship

$$n(\lambda_0) = n_{avg}. \tag{10}$$

Using a second-order Cauchy model,

$$n(\lambda) = A + \frac{B}{\lambda^2},$$

where A and B are empirical material-depending constants determined by fitting experimental data [3]. Applying $n(\lambda_0) = n_{avg}$ gives

$$n_{avg} = A + \frac{B}{\lambda_0^2} \quad \Rightarrow \quad A = n_{avg} - \frac{B}{\lambda_0^2}.$$

Therefore,

$$n(\lambda) = n_{avg} + B\left(\frac{1}{\lambda^2} - \frac{1}{\lambda_0^2}\right). \tag{11}$$

To ensure physical validity, we constrain $n(\lambda) > 1$,

$$B \in \left(0, \lambda_0^2\left(n_{avg} - 1\right)\right). \qquad (12)$$

Analysis

In the simulation, each ray is defined by an origin, a unit direction vector, and a wavelength (or a color mapped to a wavelength). The algorithm proceeds as follows.

Simulation Steps

1. Compute the closest ray–object intersection. If no intersection exists, terminate.

2. Compute $\hat{k} = (\hat{n} \times \hat{v}_1) \times \hat{n}$ using the interface normal $\hat{n}$ and incident direction $\hat{v}_1$.

3. Compute the refractive index of the second medium using the dispersion model:

$$n_2 = n(\lambda) = n_{avg} + B\left(\frac{1}{\lambda^2} - \frac{1}{\lambda_0^2}\right),$$

where $\lambda_0 = 0.589\,\mu m$ (equivalently $589\,nm$).

4. Compute

$$M = \frac{n_1}{n_2}\left(\hat{v}_1 \cdot \hat{k}\right).$$

5. Compute both outgoing directions:

$$\hat{v}_{2t} = M\hat{k} - \hat{n}\sqrt{1 - M^2}, \qquad \hat{v}_{2r} = \hat{v}_1 - 2(\hat{v}_1 \cdot \hat{n})\hat{n}.$$

If $|M| > 1$, compute only $\hat{v}_{2r}$ (TIR).

6. If refraction occurs, compute Fresnel reflectances R_s and R_p, then compute

$$R = \frac{R_s + R_p}{2}, \qquad T = 1 - R,$$

and split intensity accordingly.

7. Emit a reflected ray with intensity multiplied by R and a transmitted ray with intensity multiplied by T. Continue until termination conditions are met (no intersection or a maximum step count).

Results

Implementing the algorithm above (combined with standard light-transport routines) in a simulator written in C++ and GLSL produces a simple but functional refractive renderer. To evaluate the behavior of the model, a spherical lens rendered by the simulator is compared qualitatively against a reference render produced in Blender.

Several similarities and differences are observed. First, both renders show the lens inverting the background, and this effect is reproduced by the simulator. Second, both renders show reflections on the sphere, but the reflection region appears smaller in the simulator output. Finally, the overall brightness differs between the two renders.

Figure 1. Image produced with our method.

Figure 2. Image produced with Blender.

The background inversion indicates that the simulated refraction and reflection directions produced by the vector model are broadly consistent with expected optical behavior, suggesting that the vector forms derived from Snell's law and specular reflection are correctly implemented.

The smaller reflection region may result from differences in Fresnel implementation, since Fresnel determines how much light is reflected versus transmitted. It may also come from differences in how Blender and the simulator handle reflection events (for example, probabilistic versus deterministic decisions). In addition, small differences in

refractive index values between the two setups can affect both the size and intensity of reflections.

Because the brightness difference appears across the entire image, including regions where refraction should have minimal effect, it is likely caused by differences in post-processing or tone mapping between the two pipelines. Blender typically applies additional processing steps that increase perceptual realism, which are not included in the simulator. Therefore, this brightness difference is not directly attributable to the refraction model itself.

Although multiple optical effects are reproduced, chromatic dispersion was not implemented in the simulator. Dispersion would require splitting light into multiple rays (e.g., red, green, and blue) and propagating them through the scene. This typically requires recursive ray tracing. Since recursion is not supported in GLSL in the chosen implementation, the simulator processes one ray at a time, preventing simultaneous propagation of multiple secondary rays for spectral separation.

Conclusion

A fully vector-based formulation of refraction, reflection, and Fresnel effects has been derived and is suitable for simulation. The model reproduces refraction, partial reflection, and total internal reflection while avoiding explicit inverse trigonometric computations in the core vector model. Although chromatic dispersion was derived analytically, its implementation was limited by the lack of recursion support in GLSL under the chosen approach. Nevertheless, the framework provides a consistent foundation for physically based light simulation and can be extended with alternative control flow or multi-ray propagation strategies.

References

[1] Rotenberg, S. (n.d.). Fresnel Surfaces. UCSD. https://cseweb.ucsd.edu/classes/sp17/cse168-a/CSE168_03_Fresnel.pdf

[2] Gallegos, J., Stokkermans, T. J. (2023). Refractive Index. StatPearls Publishing. https://www.ncbi.nlm.nih.gov/books/NBK592413/

[3] Cauchy and related empirical dispersion formulae for transparent materials. (n.d.). Horiba. https://www.horiba.com/fileadmin/uploads/Scientific/Downloads/OpticalSchool_CN/TN/ellipsometer/Cauchy_and_related_empirical_dispersion_Formulae_for_Transparent_Materials.pdf

[4] Refraction, Snell's law, and total internal reflection. (2025). Boston University. https://buphy.bu.edu/py106/notes/Refraction.html

[5] Paschotta, R. (2019). Specular Reflection. RP Photonics Encyclopedia. https://www.rp-photonics.com/specular_reflection.html

Wiener Index: Chemical Graph Theory

Harry Jia Bin Ngo

Abstract – The Wiener index is a topological index that represents the sum of distances between vertices in a graph. This paper outlines its definition, computation methods, and bounds, along with applications in modeling molecular structures.

Introduction

Topological Index

Alongside the Balaban index and Harary index, the Wiener Index is a particular topological index. These indices are tools used to analyse the behaviours of compounds on a theoretical level in chemistry. They allow for the prediction of physio-chemical properties such as the viscosity of a substance. Mathematically, the topological index is obtained from graph theory and is a numerical invariant. Translating chemical compounds into chemical graphs results in a mathematical object which we are able to analyze using graph theory. Topological indices seek to turn these chemical graphs into numbers that represent the topology of the molecular graph. These numbers allow for the study of relationships between the molecule's topology, chemical graph, reactivity, physical properties, chemical properties, and much more. The computation of the Wiener index will be explored more in depth below.

Graph Theory

Applying graph theory in chemistry results in the interdisciplinary field called molecular topology or chemical graph theory.

Graphs can be transformed into matrices. The ones that we will be using are adjacency matrices and graph distance matrices.

The adjacency matrix is a table that shows which vertices are connected by an edge (adjacent to each other). It is defined as a matrix with only 1 and 0 with the diagonal being always 0 if the graph does not contain loops. The rows and columns of the matrix represent the vertices of the graph. If the vertex on row i is adjacent to the vertex j, then the entry for that ij will be 1, otherwise it is 0.

Consider the following example:

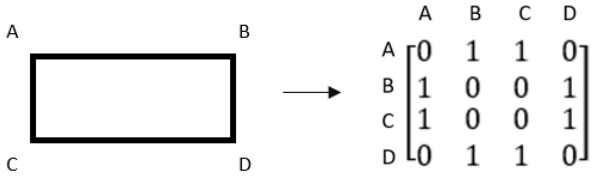

Figure 1. Adjacency matrix of the rectangle ABCD.

The distance matrix is a table that shows the distance between 2 objects (usually takes the shortest path). In our case, the 2 objects are vertices. The distance that connects the vertices in graph theory is an edge and is counted as +1 for each.

Consider the previous example:

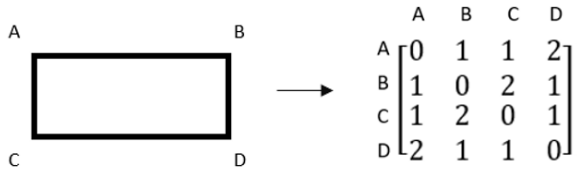

Figure 2. Distance matrix of the rectangle ABCD.

Wiener Index

Basic Definition

In chemical graph theory, the Wiener index, named after Harry Wiener, is a topological index that is defined as the sum of the minimum distance between all pairs of vertices in a finite connected graph. All edges have a weight of 1, which represents the distance between 2 vertices. We will be deriving 3 expressions for the Wiener index.

Let $G = (V, E)$ a finite connected graph, where V is the vertices, and E the edges.

Let $D_G(u, v)$ be the minimum distance (edges) between the vertices $u, v \in V$ on G.

The Wiener Index of this graph is defined as:

$$W(G) = \sum_{\{u,v\}\subseteq V} D_G(u,v) \quad (1)$$

In this definition, the path is not repeated twice. However, in some definitions of the Wiener index, it is repeated. Each edge is counted as 1 when adding the distance between 2 vertices. For example, If the shortest path uses 2 edges to connect 2 vertices, then the distance is 2.

In definition (2) of the Wiener index, when taking all the shortest possible paths, we obtain the same path twice. More precisely, it is the same path, but in opposite directions. The direction of the path is not important for the basic definition of the Wiener Index, that is why we will divide the sum of all the distances by 2.

Let $G = (V, E)$ a finite connected graph, where V is the vertices, E the Edges.

Let $D_G(v)$ be the sum of all minimum distances (edges) between v and all other vertices of G.

$$W(G) = \frac{1}{2}\sum_{v\in V} D_G(v) \quad (2)$$

The ½ is due to overcounting the same path u,v both in $D_G(v)$ and $D_G(u)$.

For facilitated computation in chemistry, use matrices.

The Wiener index would be defined as follows:

- Let G be a finite connected graph.
- Let $D_{ij}(G)$ be the distance matrix (previously defined).

The Wiener Index of this graph is defined as (based on equation 2):

$$W(G) = \frac{1}{2}\sum_{j}\sum_{i} D_{ij}(G) \quad (3)$$

We apply ½ for the same reason as equation 2.

Lower Bound

For sections 2 and 3 define G as a connected graph.

For sections 2 and3 represent $|V(G)|$, $|E(G)|$ by the variables n and m respectively.

From this, we can derive the following inequality:

$$W(G) \le W(T) \quad (4)$$

This will help us find the upper and lower bounds.

The lower bound of the Wiener index of a connected graph G is given by:

$$W(G) \ge \frac{n(n-1)}{2} \quad (5)$$

Proof:

K_n is a complete Graph.

For a finite connected graph (lower than T), the lowest Wiener index is when all the vertices are connected, such that it is a complete graph K_n. That is because the distance between all vertices is 1 in a complete graph. This means that a finite connected graph with n vertices will have the lowest Winer index if these n vertices are configured as a complete graph K_n. This is the reason why we take the complete graph to find the lower bound of the Wiener index.

$$W(G) \ge W(K_n) \quad (6)$$

In a complete graph the Wiener index is defined as:

$$W(K_n) = \frac{n(n-1)}{2} \quad (7)$$

Lemma: For any complete graph K_n, the Wiener index can be defined as:

$$\frac{n(n-1)}{2} \quad (8)$$

Use definition 3 to prove this:

$$W(K_n) = \frac{1}{2}\sum_{j}\sum_{i} D_{ij}(K_n) \quad (9)$$

$$D_{ij}(K_n) = \begin{bmatrix} 0 & \cdots & 1 \\ \vdots & \ddots & \vdots \\ 1 & \cdots & 0 \end{bmatrix} \quad (10)$$

In this matrix, all entries are 1 except the diagonal. $D_{ij}(K_n)$ is of size n x n.

Add up all the entries in the rows.

$$\sum_{i} D_{ij}(K_n) = \sum_{i} \begin{bmatrix} 0 & \cdots & 1 \\ \vdots & \ddots & \vdots \\ 1 & \cdots & 0 \end{bmatrix}$$

$$= [n-1 \;\; n-1 \;\; n-1 \cdots \; n-1] \quad (11)$$

$\sum_i D_{ij}(K_n)$ is of size n x 1.

$$\sum_j \sum_i D_{ij}(K_n) = \sum_j [n-1 \;\; n-1 \;\; n-1 \cdots n-1]$$

$$= n(n-1) \tag{12}$$

$$\frac{1}{2}\sum_j \sum_i D_{ij}(K_n) = \frac{1}{2}\, n(n-1)$$

$$W(K_n) = \frac{1}{2}\, n(n-1) \tag{13}$$

$$W(K_n) = \frac{n(n-1)}{2} \tag{14}$$

Because K_n gives the lowest Wiener index for n vertices, a connected graph with n vertices cannot be lower than the Wiener index of K_n. That is why, for any connected graph G, the lower bound for the Wiener index is defined as follows:

$$W(G) \geq \frac{n(n-1)}{2} \tag{15}$$

In section 3, the lower bound is defined slightly differently.

$$W(G) \geq n(n-1) - m \tag{16}$$

Proof:

Take vertices u, v. If they are neighbors, then $D_G(u,v) = 1$. Otherwise, $D_G(u,v) \geq 2$. Use counting to find the minimum Wiener index for G:

- In graph G, there are exactly m pairs of neighbors. Each neighbor has a distance of 1.
- In graph G, there are exactly $(n\ 2\ )$ different unordered pairs of vertices u,v in total (including the neighbors). Each pair of vertices (not neighbors) has at least a distance of 2.

From this, we can find an expression for the lower bound:

$$W(G) \geq m + 2((n\ 2\ ) - m)$$

$$W(G) \geq n(n-1) - m \tag{17}$$

Upper Bound

The lower and upper bound of the Wiener index of a connected graph G is given by:

$$n(n-1) - m \leq W(G) \leq \frac{n^3 + 5n - 6}{6} - m \tag{18}$$

The left side of the inequality (the lower bound) has already been proven in section 2. Prove the right side of the inequality (the upper bound).

$$W(G) \leq \frac{n^3 + 5n - 6}{6} - m \tag{19}$$

Proof:

P_n is the path graph (linear):

For a finite connected graph, the highest Wiener index is when all the vertices are connected in a line. That is because the distance is the highest between 2 vertices when taking the distance between the first vertex of the line and the end vertex of the line. This means that a finite connected graph with n vertices will have the highest Wiener index possible if these n vertices are configured in a line. This is the reason why we take P_n to find the upper bound of the Wiener index.

$$W(G) \leq W(P_n) \tag{20}$$

In a path graph, the Wiener index is defined as:

$$W(P_n) = \frac{n^3 - n}{6} = \frac{n^3 + 5n - 6}{6} - m \tag{21}$$

Lemma: For any complete graph P_n, the Wiener index can be defined as $\frac{n^3-n}{6} = \frac{n^3+5n-6}{6} - m$.

Use definition 3 to prove this:

$$W(P_n) = \frac{1}{2}\sum_j \sum_i D_{ij}(K_n) \tag{22}$$

$$D_{ij}(P_n) = \begin{bmatrix} 0 & 1 & 2 & 3 & \cdots & n-1 \\ 1 & 0 & 1 & 2 & \cdots & n-2 \\ 2 & 1 & 0 & 1 & \cdots & n-3 \\ 3 & 2 & 1 & 0 & \cdots & n-4 \\ \vdots & \vdots & \vdots & \vdots & \ddots & \vdots \\ n-1 & n-2 & n-3 & n-4 & \cdots & 0 \end{bmatrix}$$

The diagonal is 0.

$D_{ij}(K_n)$ is size n x n.

Add up all the entries in the rows.

$$\sum_i D_{ij}(P_n) = B_{(k)} \tag{23}$$

$$= 2\sum_i \begin{bmatrix} 0 & 1 & 2 & 3 & \cdots & n-1 \\ 1 & 0 & 1 & 2 & \cdots & n-2 \\ 2 & 1 & 0 & 1 & \cdots & n-3 \\ 3 & 2 & 1 & 0 & \cdots & n-4 \\ \vdots & \vdots & \vdots & \vdots & \ddots & \vdots \\ n-1 & n-2 & n-3 & n-4 & \cdots & 0 \end{bmatrix}$$

$$= 2\left[\sum_{n=1}^{n-1} n \ \sum_{n=1}^{n-2} n \ \sum_{n=1}^{n-3} n \ \ldots \sum_{n=1}^{n-n} n \ \right] \quad (24)$$

$$\sum_i D_{ij}(P_n) \ is\ of\ size\ n \times 1$$

$$\frac{1}{2}\sum_j \sum_i D_{ij}(P_n) \quad (25)$$

$$= \frac{1}{2} \cdot 2\sum_j \left[\left(\sum_{n=1}^{n-1} n\right)\left(\sum_{n=1}^{n-2} n\right)\left(\sum_{n=1}^{n-3} n\right)\ldots\left(\sum_{n=1}^{n-n} n\right)\right]$$

$$= \sum_{i=1}^{n}\sum_{n=1}^{n-i} n \quad (26)$$

$$\frac{1}{2}\sum_j \sum_i D_{ij}(P_n) \ = \sum_{i=1}^{n}\sum_{n=1}^{n-i} n \quad (27)$$

$$W(P_n) = \sum_{i=1}^{n} \frac{(n-i)(n-i+1)}{2} \quad (28)$$

$$W(P_n) = \sum_{i=1}^{n} \frac{n^2 - 2in + n + i^2 - i}{2}$$

$$W(P_n) = \frac{1}{2}\sum_{i=1}^{n} n^2 - 2in + n + i^2 - i$$

$$W(P_n) = \frac{1}{2}\left(\sum_{i=1}^{n} n^2 - \sum_{i=1}^{n} 2in + \sum_{i=1}^{n} n \ + \sum_{i=1}^{n} i^2 - \sum_{i=1}^{n} i \ \right) \quad (29)$$

Evaluate each sum and expand everything:

$$W(P_n) = \frac{1}{2}(n^3 - (n^3 + n^2) + n^2 + \frac{2n^3+3n^2+n}{6} - \frac{n^2+n}{2})$$

$$W(P_n) = \frac{1}{2}(\frac{2n^3 + 3n^2 + n}{6} - \frac{n^2 + n}{2})$$

$$W(P_n) = \frac{n^3-n}{6} \quad (30)$$

In P_n, $m = n - 1$

$$W(P_n) = \frac{n^3+5n-6}{6} - (n-1) \quad (31)$$

$$W(P_n) = \frac{n^3+5n-6}{6} - m \quad (32)$$

Because P_n gives the highest Wiener index for n vertices, a connected graph with n vertices cannot be higher than the Wiener index of P_n. That is why, for any connected graph G, the upper bound for the Wiener index is defined as follows:

$$W(G) \leq \frac{n^3 + 5n - 6}{6} - m \quad (33)$$

Now that both the upper and lower bounds have been proven, the bounds for the Wiener index can be summarized by:

$$n(n-1) - m \leq W(G) \leq \frac{n^3+5n-6}{6} - m \quad (34)$$

Wiener Index in Chemistry and Applications

Linear Compounds

The Wiener Index was originally created by a chemist for alkane molecules. Alkane molecules are molecules that are non-cyclic and that are fully saturated. As previously explained, the calculation of the Wiener index will be done using a distance matrix. In addition, the vertices will be the carbon atom, and the edges will be the carbon-carbon single bond (C-C). The hydrogen bonds are ignored in the Wiener index; only the carbon bonds are considered.

Consider the following example: n-butane.

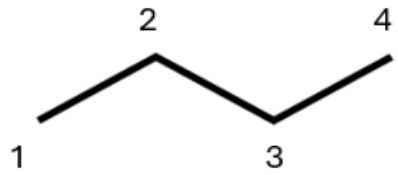

Figure 3. Skeletal structure of n-butane.

To calculate the Wiener Index, find the sum of the distances (edge or C-C) of all paths between carbon atoms. The distance of C-C = 1 since they are considered edges, and based on the definition of the distance matrix, each edge = 1.

$1 \rightarrow 2 = 1$ $1 \rightarrow 3 = 2$ $1 \rightarrow 4 = 3$

$2 \rightarrow 3 = 1$ $2 \rightarrow 4 = 2$

$3 \rightarrow 4 = 1$

From the definition of the Wiener index, this would be the half we take into consideration, but if we consider ALL paths:

$4 \rightarrow 3 = 1$ $4 \rightarrow 2 = 2$ $4 \rightarrow 1 = 3$

$3 \rightarrow 2 = 1$ $3 \rightarrow 1 = 2$

$2 \rightarrow 1 = 1$

Because the paths are the same as the ones above, these paths are not summed up (equivalent to dividing by 2).

Summing up the distances, we get:

$$(3 \times 1) + (2 \times 2) + (1 \times 3) = 10$$

The Wiener index for n-butane is 10.

The Wiener index can be computed depending on the kind of molecules we are dealing with. More precisely, it depends on the molecular graph which represents the molecule. If this graph is linear, it is possible to calculate it easily (shown below), but if it was substituted, which is the equivalent of a simple connected graph, then it will most likely be calculated using the matrix definition of the Wiener index. It is most likely possible for a cyclic graph C_n as well, but it is not proven in this paper.

For linear (P_n): proof is shown in section Upper Bound

$$W(P_n) = \frac{n^3 - n}{6}$$

Plug in n = 4 for butane and you would see that $W(P_4) = 10$.

Algorithms

The good news is that molecules cannot form infinitely long chains. There is a limit to how many neighbors a carbon atom can have (max 4). This means that molecules are finite and can be computed using the distance matrix. The time complexity of the algorithm for the Wiener index is O(mn) where m is the number of edges and n is the number of vertices.

Most algorithms that calculate the Wiener index use a distance matrix in some way. Bojan Mohar and Tomaz Piskanski's "How to Compute the Wiener Index of a Graph" discusses the possibility of calculating the Wiener index without the distance matrix, possibly a shorter way of computing it.

References

[1] N. S. Schmuck, (2010). *The Wiener index of a graph* [Diploma thesis]. Graz University of Technology, https://www.math.tugraz.at/~schmuck/publications/Diplomarbeit.pdf

[2] B. Mohar, T. Pisanski, *How to Compute the Wiener Index of a Graph*, in Journal of Mathematical Chemistry, vol. 2, 1987. https://users.fmf.uni-lj.si/mohar/Reprints/1988/BM88_JMC2_Pisanki_WienerIndex.pdf

[3] M. S. Abdelgader, C. Wang, S. A. Mohammed, *Computation of Topological Indices of Some Special Graphs*, in Mathematics, vol. 6, issue 3, 2018. https://www.mdpi.com/2227-7390/6/3/33

[4] P. Dankelmann, *Proof of a conjecture on the Wiener index of Eulerian graphs*, in Discrete Applied Mathematics, vol. 301, p.99-108, 2021. https://www.sciencedirect.com/science/article/pii/S0166218X21001876

[5] S. Nikolic, N. Trinajstic, Z. Mihalic, *The Wiener Index: Development and Applications*, in Croatica Chemica Acta, vol. 68, issue 1, p.105-129, 1995. https://www.researchgate.net/publication/263274230_The_Wiener_Index_Development_and_Applications

About DrJes

The Dawson Research Journal of Experimental Science (DrJes) is a student publication of Dawson College's Science Program. Its aim is to publish experimental research undertaken by college students, either independently or as part of their program of study. Inquiries should be sent to the addresses provided below. For past editions, please visit the DrJes webpage.

Contact

E-mail

Andrew Stewart (Science Activities Coordinator)
anstewart@dawsoncollege.qc.ca

Mailing Address

The Dawson Research Journal of Experimental Science (DrJes) c/o Andrew Stewart
3040 Sherbrooke St. West, Suite 6B.17-1
Montreal, QC, H3Z 1A4, Canada

Webpage

https://www.dawsoncollege.qc.ca/drjes/issues/